

# Distinct local and brain-wide networks are activated by layer-specific optogenetic stimulations of motor cortex

**Russell Chan**

The University of Hong Kong

**Mazen Asaad**

Stanford University

**Bradley Edelman**

Stanford University <https://orcid.org/0000-0002-7502-9620>

**Hyun Joo Lee**

Stanford University

**Hillel Adesnik**

University of California, Berkeley <https://orcid.org/0000-0002-3796-8643>

**David Feinberg**

University of California, Berkeley

**Jin Hyung Lee** (✉ [ljinhy@stanford.edu](mailto:ljinhy@stanford.edu))

Stanford University

---

## Article

**Keywords:** optogenetic stimulation, motor cortex, brain-wide networks

**Posted Date:** December 3rd, 2020

**DOI:** <https://doi.org/10.21203/rs.3.rs-115504/v1>

**License:** © ⓘ This work is licensed under a Creative Commons Attribution 4.0 International License.

[Read Full License](#)

---

# Abstract

Primary motor cortex consists of a stack of interconnected but distinct layers, and plays a prominent role in motor control through large-scale networks. However, differential effects of M1 layer-specific functional pathways remain elusive, especially at the macroscopic and mesoscopic scales. Here, we combined layer-specific Cre-driver mouse lines, optogenetics, and fMRI with electrophysiological recordings to identify distinct M1 layer-specific networks. Neuronal activities initiated in L2/3 were mainly confined within M1, while stimulation of L4, L5, and L6 evoked distinct responses in M1 and motor-related subcortical regions, including the striatum and motor thalamus. Although motor cortex has long been considered agranular (without L4), our results structurally, functionally, and neurovascularly confirm the presence of L4. We also find that layer-specific fMRI responses closely couple with laminar electrophysiological recordings. Overall, our results elucidate distinct brain-wide neural archetypes of M1 layer-specific cortical circuits that provide important insights in uncovering the motor system architecture.

## Introduction

Primary motor cortex (M1) plays a prominent role in motor behavior and the cortical control of movements through large-scale networks. Long-range inputs converge onto M1 through cortico-cortical, thalamo-cortical and neuromodulatory projections, while M1 outputs project to spinal/bulbar motor centers, striatum, thalamus, subthalamus, red nucleus, and pons<sup>1,2</sup>. Like the sensory cortices, M1 consists of a stack of interconnected but distinct layers. Traditionally, layers 2/3 (L2/3) are considered to be a prominent source of intracortical excitation of L5<sup>3,4</sup>. Additionally, L5 has output connections to the ventral anterior thalamus (VA), striatum and spinal cord, while L6 has output connections to the ventral lateral thalamus (VL)<sup>3</sup>. Recently, L4 has been proposed to have prototypical synaptic circuit connectivity<sup>5</sup>. Despite this seemingly well-defined structural organization, the brain-wide functional influences of M1 layer-specific pathways have yet to be elucidated at the whole-brain scale.

Historically, it has been difficult to disentangle the functional properties of different cortical layers as they are highly anatomically intermingled. However, some neurons that constitute layer-specific pathways share relatively distinct neurochemical identities, suggesting that the activation of such discretized layers may result in highly dissimilar brain-wide responses. In particular, some neurons in L2/3, L4, L5, and L6 of the neocortex express the dopamine receptor D3 (Drd3), the sodium channel non-voltage-gated 1 alpha (Scnn1a), the RNA polymerase II subunit B32 (Rpb4) and the neurotensin receptor type 1 (Nstr1), respectively. Advances in molecular genetics, such as the advent of Cre-recombinase driver lines<sup>6</sup> and optogenetic tools<sup>7</sup>, have thus made it possible to selectively express transgenes in the various neocortical layers. Several studies have exploited this capability to selectively excite specific layers and measure the downstream effects using *in vivo* electrophysiology. For example, in the somatosensory cortex, L2/3 was shown to suppress L5 to enhance the selectivity and output range of downstream activity for finely-tuned cortical coding<sup>8</sup>. L4 activity of the somatosensory cortex was also shown to directly inhibit L5 to sharpen the spatial representation of L5 neurons<sup>9</sup>. In addition, L6 corticothalamic neurons in the visual cortex

have been shown to activate L5 cortical outputs<sup>10</sup> and to regulate the strength of cortical responses<sup>11</sup>. These studies have mainly characterized the downstream activities within the cortex, while only a few L5 studies have investigated long-range pathways such as the corticotectal projections in the visual system<sup>12</sup> and the corticofugal projection in the auditory system<sup>13</sup>. Furthermore, these studies have focused on the sensory cortices (auditory, somatosensory and visual cortices), which are structurally and functionally distinct from M1. Since layer-specific M1 activities distinctly contribute to cortical control of movements, and since different layers in M1 have distinct contributions to motor-related dysfunctions, such as Parkinson's disease (PD), it is essential to characterize the downstream effects of layer-specific M1 excitation. However, to date, there has been no direct evidence of differential effects of M1 layer-specific pathways on brain-wide circuit function, especially at the macroscopic and mesoscopic scale.

Conventional functional MRI (fMRI) is performed at a macroscopic scale. However, recent developments in high-spatial resolution fMRI provide opportunities for *in vivo* measurements of mesoscale layer-specific cortical responses<sup>14</sup>. Laminar fMRI can be used to tackle key cognitive neuroscience questions by distinguishing bottom-up and top-down cortical responses and examining the interactions between the two<sup>15</sup>. It can also provide a robust testbed for examining influential theories of brain-wide circuit function by assigning specific computational roles to different cortical layers<sup>16</sup>. However, the mesoscale layer-specific fMRI representation of neuronal activity has not been established.

The integration of optogenetic stimulation with fMRI (ofMRI) has enabled the causal influences of genetically defined neuronal populations on downstream regions to be measured directly<sup>17-22</sup>. Here, we combined targeted optogenetic stimulation of M1 L2/3, L4, L5, and L6 with large field-of-view high-resolution fMRI to reveal the causal influences of activities originating in each layer on brain-wide regions, including different M1 layers, the thalamus, and the caudate putamen (CPu). Subsequently, we characterized these downstream region activities locally and remotely using *in vivo* electrophysiology to delineate the neuronal underpinnings of the fMRI responses. Last, we explored neuronal origins of the laminar ofMRI responses.

## Results

# Layer-specific M1 stimulations activate distinct brain-wide networks

To selectively activate L2/3, L4, L5, and L6 of primary motor cortex (M1) *in vivo*, we used transgenic mouse lines expressing Cre-recombinase<sup>9,23-25</sup> under control of *Drd3*, *Scnn1a*, *Rpb4* and *Nstr1* receptor regulatory elements, respectively. An AAV5 virus was injected into the M1 to express the excitatory opsin ChR2 in Cre-positive neurons to enable selective layer-specific optogenetic control of M1. Histological and immunohistochemical examination confirmed that ChR2-EYFP was localized to the neurons in their respective layers and their intra-cortical projections (Fig. 1). Specifically, ChR2-EYFP expression was observed in L2/3 M1 neurons and their L5 projections for the *Drd3* L2/3 Cre-line, in L4 M1 neurons and

their L2/3 projections for the Scnn1a L4 Cre-line, in L5 M1 neurons and their L2/3 projections for the Rbp4 L5 Cre-line, and in L6 M1 neurons and their L4 projections for the Ntrs1 L6 Cre-line.

Whole-brain fMRI was applied to determine layer-dependent spatiotemporal characteristics of brain-wide evoked responses driven by layer-specific M1 stimulation. Optical pulses were delivered at 5 Hz (30% pulse width duty cycle; light intensity, 30–50 mW/mm<sup>2</sup>) and a general linear model (GLM) was used to identify voxels significantly modulated during stimulation. fMRI activation maps (Fig. 2A,  $p < 0.001$ , FDR corrected,  $n = 12$ ) and blood oxygen level dependent (BOLD) signal profiles (Fig. 3A) show that layer-specific M1 stimulations at 5 Hz activate distinct brain-wide networks. Note that BOLD signal profiles were extracted using atlas-based, anatomically-defined regions of interest (ROIs; Fig. 2B). L2/3 stimulation activated only ipsilateral M1 (Figs. 2A and 3A). L4 stimulation activated ipsilateral M1, while small negative BOLD responses were observed in the contralateral M1, ipsilateral CPu and ipsilateral VL (Figs. 2A and 3A). L5 stimulation evoked robust ipsilateral M1, CPu, and VL activations, while relatively smaller BOLD responses were detected in the contralateral M1, and CPu (Figs. 2A and 3A). Note that the BOLD signal in the contralateral CPu peaks after stimulation offset (Fig. 3A). Last, L6 stimulation evoked robust VL activation (Figs. 2A and 3A). Bilateral M1 and CPu responses were also observed during L6 stimulation with the BOLD signal transitioning from negative to positive during and after stimulation (Fig. 3A).

To compare and quantify the response patterns between different layer-specific stimulations, for each atlas-based anatomically-defined ROI, we extracted the average t-values, fraction of ROI positively and negatively modulated, and calculated the area under the extracted BOLD signal profiles (Figs. 2C and 3B; one-way ANOVA, Bonferroni's post hoc test). Among the different layer-specific stimulations, L5 stimulation evoked the strongest ipsilateral M1 and bilateral CPu activations (Figs. 2C and 3B). L6 stimulation evoked the strongest ipsilateral VL activations, and L5 stimulations also evoked significantly stronger activations than L2/3 and L4 stimulations (Figs. 2C and 3B).

Since the CPu and VL were robustly activated during L5 and L6 stimulations, respectively, histology and immunohistochemistry of these regions were examined. Long-range M1 L5 and L6 projections were revealed in the CPu and VL (Supplementary Fig. 1), respectively, supporting our fMRI results. Since stimulation frequency can evoke distinct local and brain-wide responses<sup>18,21,22,26</sup>, we also applied 10, 20, and 40 Hz layer-specific M1 stimulations within the same animals to investigate frequency-dependent spatiotemporal characteristics. The responses evoked by these stimulation frequencies largely resemble responses evoked by the 5 Hz stimulation (Supplementary Fig. 2). The extracted t-values had a decreasing trend with frequency in ipsilateral M1 during L4 stimulation, while both the extracted t-values and fraction of ROI positively modulated had an increasing trend with frequency in contralateral CPu and ipsilateral VL during L5 stimulation (Fig. 2D; one-way ANOVA followed by trend analysis). For L6 stimulation, ipsilateral M1 responses had increasing trends with increasing stimulation frequency for t-values and fraction of ROI positively modulated, while a decreasing trend with frequency was observed for fraction of ROI negatively modulated (Fig. 2D; one-way ANOVA followed by trend analysis). For area under the curve of the BOLD signal, they showed an increasing trend in ipsilateral M1 during L5 and L6

stimulations, as well as ipsilateral CPU and VL during L5 stimulation (Fig. 3C; one-way ANOVA followed by trend analysis). In addition, the BOLD signal in the ipsilateral M1 transitioned from negative to positive during 5 and 10 Hz L6 stimulations, but not 20 and 40 Hz stimulations (Supplementary Fig. 3A). No evoked responses were observed in a naïve animal (Supplementary Fig. 4), indicating that the observed responses were a direct consequence of ChR2 stimulation rather than heat induced artifacts or undesired light-induced activations<sup>27,28</sup>.

## Neuronal underpinnings of the brain-wide fMRI responses

To investigate how layer dependent fMRI responses relate to neuronal activity, we obtained simultaneous *in vivo* extracellular recordings in ipsilateral M1, CPU, and VL under the same conditions as the ofMRI experiments (5 Hz stimulations: Figs. 4 and 5; 10, 20, and 40 Hz stimulations: Supplementary Figs. 5 and 6;  $n = 4$  for each layer-specific Cre-line). Local field potential (LFP) recordings revealed that L2/3 stimulation mainly evoked responses in ipsilateral M1 (Fig. 4B and Supplementary Fig. 5A). On the other hand, L4, L5 and L6 stimulations evoked distinct LFP responses in the ipsilateral M1, CPU, and VL (Fig. 4B and Supplementary Fig. 5A). Furthermore, the evoked LFP responses in the ipsilateral M1 and VL had the strongest change in LFP amplitude during L5 and L6 stimulations, respectively (Fig. 3C), matching our fMRI results (Figs. 2 and 3). The scatter plot also demonstrates that the evoked LFP responses are closely correlated with the BOLD-fMRI responses (Fig. 4D). The amplitude of the LFP responses generally decreased with stimulation frequency in all four layer-specific stimulations (Supplementary Fig. 5C). Note the LFP responses at the beginning of the stimulation were similar across stimulation frequencies within each layer-specific Cre-line (Supplementary Fig. 5A).

Since the BOLD signal is thought to be associated with spiking output, we also analyzed the spike recordings in ipsilateral M1, CPU, and VL. Across all recorded units, over half of the units were modulated by the stimulation of all layers (Fig. 5A and Supplementary Table 1;  $n = 4$  for each layer-specific Cre-line; 20 trials per frequency per animal). Most modulated units exhibited a significant increase in firing rate except for those in the ipsilateral VL during L5 and L6 stimulations (Fig. 5A and Supplementary Table 2). Among the units with significantly increased firing rates, the spike rates in the ipsilateral M1, CPU, and VL significantly increased during L2/3, L4, L5, and L6 stimulations at all frequencies (Fig. 5C and Supplementary Fig. 6E;  $p < 0.001$ ; one-way ANOVA, Bonferroni's post hoc test). Since BOLD-fMRI and LFP responses reflects large scale net activity within a region, we considered all recorded units when exploring the association between spiking, BOLD-fMRI, and LFP. The scatter plots show that the total absolute value of % spike rate change of all neurons is correlated with BOLD-fMRI and LFP responses (Fig. 5D and Supplementary Fig. 6H & 6I). Some units exhibited a significant decrease in firing rate in the ipsilateral VL during L5 and L6 stimulations (Fig. 5A, Supplementary Fig. 6A, 6F and 6G, and Supplementary Table 3). No evoked responses were observed in the naïve animal (Supplementary Fig. 7), indicating that the observed responses were direct consequences of ChR2 stimulation and not photovoltaic induced artifacts or undesired light-induced activations<sup>29,30</sup>.

## Layer-specific fMRI responses and their neuronal origins

To examine layer-specific fMRI representation of neuronal activity, we first analyzed the local fMRI responses during layer-specific M1 stimulations. Local fMRI activation maps (Fig. 6A;  $p < 0.001$ , FDR corrected,  $n = 12$ ) and BOLD signal profiles extracted from atlas-based anatomically-defined ROIs show that layer-specific M1 stimulation activates distinct local responses (Fig. 6D). Interestingly, all fMRI responses exhibit an increasing trend along the cortical depth (Fig. 6B; one-way ANOVA followed by trend analysis). Parts of the ROI positively modulated exhibit an increasing trend along the cortical depth during L4 and L5 stimulations, while parts of the ROI negatively modulated exhibit a decreasing trend along the cortical depth during L4 stimulation (Fig. 6C; one-way ANOVA followed by trend analysis). BOLD signal (Fig. 6D) area under the curve exhibit an increasing trend along the cortical depth during L5 and L6 stimulations (Fig. 6E; one-way ANOVA followed by trend analysis). Similar results were obtained during 10, 20, and 40 Hz layer-specific stimulations (Supplementary Fig. 8). Notably, during L6 stimulation, the BOLD signal shows initial negative response, which reduces with cortical depth (Fig. 6D) and higher stimulation frequency (Supplementary Fig. 8D).

To understand the neuronal origins of such layer-specific fMRI responses, we analyzed *in vivo* extracellular recordings obtained along the M1 cortical depth (Figs. 7 and 8). Surprisingly, the LFP amplitude decreased along the cortical depth during L2/3 and L5 stimulations, while the amplitude increased along the cortical depth during L6 stimulation (Fig. 7B and 7C). The discrepancy between the fMRI and LFP response trend across layers during stimulation of each layers potentially point to layer-specific neurovascular coupling mechanisms. Scatter plot shows the overall correlation between the LFP and the laminar BOLD-fMRI signal across all four cortical layer stimulations and resulting responses in all layers (Fig. 7D). The amplitude of the LFP responses generally decreased with stimulation frequency with all four layer-specific stimulations (Supplementary Fig. 9C). LFP responses at the beginning of the stimulation was similar across stimulation frequencies (Supplementary Fig. 9A). We also examined neuronal spiking activity along the M1 cortical depth in response to M1 layer-specific stimulations (Fig. 8). Over half of all recorded units were modulated by the selective stimulation of each layer (Fig. 8A and Supplementary Table 4;  $n = 4$  for each layer-specific Cre-line, 20 trials per frequency per animal). Furthermore, nearly all modulated units exhibited a significant increase in firing rate (Fig. 8A and Supplementary Tables 5 and 6; 4 animals per layer-specific stimulation, 20 trials per frequency per animal). The spike rates significantly increased in all layers during L5 and L6 stimulations (Fig. 8C; one-way ANOVA, Bonferroni's post hoc test). The scatter plots shows the correlations between the spike rate, the laminar BOLD-fMRI signal, and the LFP along the cortical depth (Fig. 8D and Supplementary Fig. 10).

## Discussion

Here, we combined layer-specific Cre-driver mouse lines, optogenetics, and large-view fMRI with subsequent electrophysiological recordings to reveal distinct brain-wide (Fig. 2–5) and local (Fig. 6–8) M1 layer-specific networks. These techniques enable investigations of the mechanisms of both local and brain-wide layer-specific cortical circuit functional changes during development, aging, diseases and pharmacological interventions in future studies. In particular, how different cortical layers contribute to the local networks, and how these local networks contribute to brain-wide functional networks in normal

and diseased state should be addressed. For instance, our results show that laminar BOLD-fMRI (Fig. 6), LFP (Fig. 7), and spike (Fig. 8) responses were mainly confined within the deeper layers (L5 and L6) of M1 during L2/3 stimulations while L5 stimulations evoked strong responses in all layers. Globally, our results show that BOLD (Figs. 2 and 3), LFP (Fig. 4), and spike (Fig. 5) responses were mainly confined within M1 during L2/3 stimulations, while L5 stimulations evoked local (M1) and brain-wide (CPu and VL) responses. Therefore, where L5 stimulation appeared to generate widespread activation both within and outside of M1, L2/3 activation imposed local and global bounds on neural activation. Since L2/3 of the somatosensory cortex can suppress L5<sup>8</sup>, we speculate that L2/3 stimulation similarly limited activity in the deeper layers of M1 and inhibited downstream propagation to regions such as the CPu and VL. Future studies may address the role(s) of each layer in coordinating and gating large-scale motor networks.

Traditionally, M1 is an agranular cortical area which features a lack of cytologically distinct L4<sup>31,32</sup>. The existence of a M1 L4 has emerged from previous studies as one that is composed of a thin band of pyramidal cells<sup>33,34</sup> and with thalamic afferents innervated at the middle of M1<sup>35,36</sup>. These concepts are in contrast to the traditional view of M1 layer architecture and has only been recently challenged with the reporting of a functional L4<sup>5,37</sup>. Our fluorescence images show ChR2-EYFP expression in L4 neurons for the Scnn1a Cre-line mice in M1 (Fig. 1B – D), and the thickness of the expression in L4 was ~ 100  $\mu$ m (Fig. 1B – C) which is consistent with previous reports<sup>5</sup>. ChR2-EYFP expression was observed in L2/3 projections from L4 and is also consistent with the previous study<sup>5</sup>. From a functional perspective, our electrophysiological recordings demonstrate that M1 L4 responses can be evoked by L4 optogenetic stimulation, or by that of L2/3, L5 or L6 (Figs. 7 and 8). Activities initiated from M1 L4 can even propagate downstream to the CPu and VL (Figs. 4 and 5). Furthermore, these neuronal responses parallel the fMRI responses which are connected through neurovascular coupling (Figs. 2–5). Our histology, electrophysiological recordings, and ofMRI results support the presence of L4 in M1 structurally, functionally, and neurovascularly, which facilitates future studies to focus on what types of information M1 L4 neurons process, how they do so, and how this relates to motor behavior in healthy, development, aging, and disease states.

Parkinson's disease (PD) is a progressive neurodegenerative disorder that affects movement. Although striatal dopamine deficiency caused by neuronal loss in the substantia nigra has been one of the hallmarks of PD<sup>38–40</sup>, recent evidence demonstrated that the motor cortex plays a prominent role<sup>41–43</sup>. Furthermore, some studies indicate that M1 is fundamental to the pathophysiology of PD which propagates along the cortico-striatal-thalamo-cortical network<sup>38,41,43</sup>. Since motor cortex consists of different layers, it is imperative to study how different layers in M1 contribute to PD. Previous post-mortem studies have shown that PD patients have decreased M1 cortical thickness with ~ 70% reduction in L1 and L3, and with 25% reduction in L6<sup>41,44</sup>. However, the layer-specific M1 local and brain-wide circuit function alterations in PD remain largely unknown. Our results demonstrate that L5 and L6 M1 activities propagate to the CPu and VL (Fig. 2–5), which indicates that these layers directly influence the cortico-striatal-thalamo-cortical network. Additionally, we show that neuronal activity initiated in different layers

results in distinct local networks (Fig. 6–8), yet how these local networks affect cortico-striatal-thalamo-cortical network remain unknown. Future studies may utilize layer-specific ofMRI to study different PD animal models to understand and characterize local and brain-wide layer-specific circuit dysfunction, and the interactions between the local and global networks in PD. Subsequent electrophysiological recordings can explore the neural origins of these networks, and ultimately establish foundations for early diagnosis and treatment of Parkinson's disease.

A better understanding of the contribution of the motor cortex to PD symptoms will facilitate the development of novel therapeutic approaches. Subthalamic nucleus (STN) deep brain stimulation (DBS) has been recognized as a therapeutic method for PD<sup>45</sup>, yet many patients are reluctant to undergo invasive procedures or are not eligible. Recent studies have explored non-invasive methods using transcranial magnetic stimulation<sup>46–49</sup> and pharmacological modulation<sup>50</sup> of the motor cortex. However, these methods have not been proven to be reliable, partly due to the non-specific stimulation and modulation of the whole motor cortex. Nevertheless, these studies suggest that TMS and pharmacological modulation of the motor cortex can induce striatal DA release which attenuate PD symptoms. Moreover, 120 Hz stimulation of the M1 L5 cells attenuated PD symptoms in parkinsonian rodent model<sup>51</sup>. Our results demonstrate that L5 stimulations evoked striatal responses (Figs. 2–5). Taken together with the previous studies, our study results show that L5 layer-specific stimulations can potentially be used as a neuromodulation technique for PD treatment.

Motor cortex stimulation is also used as a treatment for chronic neuropathic pain<sup>52–54</sup> or for rehabilitation after stroke<sup>55–57</sup>, but with mixed success. One limitation of motor cortex stimulation is that it cannot separately modulate different layers or different neuronal elements within a region. This makes it difficult to identify the exact mechanisms of different motor cortex stimulation paradigms. By using optogenetics to selectively stimulate different layers of M1, we found that each layer drives unique local and brain-wide responses. Future studies interested in therapeutic applications may wish to investigate particular layers within this circuit. We also show that the stimulation of layer-specific M1 can drive distinct effects depending on the precise frequency used. Frequency can be a key parameter in optimizing the efficacy of motor cortex stimulation, and our current and past studies illustrate this effect.

The sensory cortex is heterogeneous with differential functions that include visual, auditory and somatosensory processing, and similarly consists of a stack of six interconnected but distinct layers<sup>31</sup>. Although the current study mapped the propagation of layer-specific M1 activities, the propagation of sensory cortical activities is yet to be characterized. Future studies may determine the specific spatiotemporal propagation of layer-specific sensory cortical activities using layer-specific ofMRI. Furthermore, the mesoscale fMRI representation of neuronal activity can also be established in the sensory cortices, which can provide foundations for studying the alterations of local and brain-wide layer-specific cortical networks in different neurodegenerative diseases. In addition, cognitive functions, such as memory acquisition, memory consolidation, and memory retrieval, involves in complex brain functional networks<sup>58,59</sup>. However, how different cortical layers are involved in these processes remains

largely unknown. Layer-specific fMRI may be applied to characterize and explore the spatiotemporal dynamics and functional roles of these cognitive networks.

The nature of neurovascular coupling remains an active area of research<sup>60,61</sup> with various studies suggesting that positive BOLD signals reflect increases in synaptic input<sup>62</sup> and others linking the BOLD signal to spiking activity<sup>17,18,63</sup>. In the current study we examined the neurovascular coupling in response to layer-specific M1 stimulation in core motor-related regions such as the cortex, striatum and thalamus. Overall, the temporally resolved coupling between neuronal spiking/LFP and the BOLD response was region specific. We showed that positive BOLD responses in the ipsilateral M1 correspond to negative peaks of the LFP responses (Supplementary Fig. 11) and the increase in spiking for all layer-specific stimulations, which is consistent with various neurovascular coupling studies<sup>17,18,60,62,63</sup>. For the ipsilateral CPu, we found that a negative and positive BOLD response were respectively linked to positive and negative peaks of the LFP during L4 and L5 stimulations (Supplementary Fig. 11), respectively. Specifically, L6 stimulations evoked BOLD responses that transitioned from negative to positive which corresponded to a similar transition of the LFP response from positive peaks to negative peaks (Supplementary Fig. 11). Furthermore, all layer-specific stimulations resulted in a spiking increase in the ipsilateral CPu, even though L2/3 and L4 stimulation evoked no and negative BOLD responses, respectively. These ipsilateral CPu results suggest that the BOLD and LFP responses inversely covary, while changes in spiking might not be highly correlated to the BOLD response. These CPu results are supported by previous striatal studies which show that negative BOLD is associated with large increases in neuronal activities<sup>64-66</sup>. For the ipsilateral VL, on the other hand, we found that both positive and negative BOLD responses were linked to positive LFP peaks for L4, L5 and L6 stimulations (Supplementary Fig. 11; L2/3 stimulation resulted in no BOLD nor LFP responses). Unchanged or negative BOLD responses corresponded to a spiking increase in the ipsilateral VL during L2/3 and L4 stimulations, while positive BOLD corresponded to a mix of spiking increase and decrease in different units during L5 and L6 stimulations. While the neurovascular coupling properties varied by region in the current work, additional studies using simultaneous fMRI and electrophysiological recordings should be performed to elucidate region- and/or layer-specific relationships.

More recently, neurovascular coupling research has expanded to using mesoscale laminar fMRI methods<sup>14,67</sup>. Among the M1 cortical layers in mice, L4 is considered the thinnest at  $\sim 100 \mu\text{m}$  and L5 and L6 the thickest at  $\sim 300 \mu\text{m}$ <sup>5</sup>. While resolving these thicknesses approaches the limitations of the spatial resolution of fMRI, we attempted to establish the mesoscale layer-specific representation of neuron activity. Although layer-specific fMRI responses were distinct during L2/3, L4, L5, and L6 stimulations, all fMRI responses increased along the cortical depth. This phenomenon, however, was not observed in the LFP and spike recordings. Despite the distinct M1 recordings that we observed during layer-specific stimulations, LFP responses and increased spiking were detected across all cortical layers. Since draining veins carry deoxygenated blood from deeper cortical layers to the surface<sup>68</sup>, L6 neurons would be the first to consume the oxygen through the supply of nearby capillaries. This would leave deoxyhemoglobin in the blood stream to be transported upwards to the superficial layers, and may cause

an initial negative or decrease in BOLD at the superficial layers. In particular, the BOLD responses transitioned from negative to positive in the superficial layers during low frequency (5 Hz – 20 Hz) L6 stimulation, and the amplitude of this initial negative BOLD response decreased along the cortical depth. This observation supports the hypothesis that draining veins transports deoxyhemoglobin from the deeper layers to the superficial layers causing an initial negative or decrease in BOLD. Our results provide insight into the feasibility of studying neurovascular coupling at the mesoscale using ofMRI. Future studies may take into account the neurovasculature to elucidate the exact mechanisms of mesoscale layer-specific neurovascular coupling.

## Materials And Methods

### Transgenic mice

Mice (CD-1, male, 35 – 50 g, N = 64 total, n = 15 for each mouse line) used for experiments in this study were heterozygous for *Drd3-Cre* (L2/3), *Scnn1-Cre* (L4), *Rpb4-Cre* (L5), or *Ntsr1-Cre* (L6). All transgenic mouse lines were obtained from the Adesnik Lab, UC Berkeley<sup>9,23-25</sup>. Mice were housed in cohorts of five or less with a light:dark cycle of 12:12 h with access to food and water *ad libitum*. All experimental procedures and animal husbandry were performed in strict accordance with the NIH and Stanford University Institutional Animal Care and Use Committee guidelines. For each transgenic mouse line, 12 were used for ofMRI, 1 for histology and immunohistochemistry, and 4 for electrophysiological recordings.

### Viral Expression and Stereotaxic Surgery

A double-floxed inverted open reading frame (DIO) recombinant AAV5 virus was used to express ChR2-EYFP in Cre-expressing neurons. The recombinant AAV vector was packaged by the University of North Carolina viral vector core (titer of  $4 \times 10^{12}$  particles/mL). All stereotaxic surgeries were performed with mice at 8 – 10 weeks of age. Animals were anesthetized with isoflurane (induction 5%, maintenance 1.5% – 2%; Sigma-Aldrich) and secured in a stereotaxic frame with nonrupturing ear bars (Kopf Instruments). A heating pad was used to maintain body temperature, and sterile ocular lubricant was applied to the eyes to prevent desiccation during surgery. Buprenorphine (1 mg/kg) was injected subcutaneously for analgesia. After a midline incision along the scalp, a small craniotomy and viral injection/cannula implantation were performed at the primary motor cortex (+ 0.75 mm AP [anterior-posterior], – 1.5 mm ML [medial-lateral], injection at + 0.15 mm, + 0.35 mm, + 0.6 mm, or + 0.8 mm DV [dorsal-ventral] for L2/3, L4, L5, and L6 respectively). 1.5  $\mu$ L of the AAV5/DIO-ChR2–EYFP virus was delivered using a 10  $\mu$ L syringe with a 34G metal needle (World Precision Instruments Inc.) at a 75 nL/min flow rate driven by a micro-syringe pump controller. Following injection, the injection needle was held in place for 10 min before slowly retracting it from the brain. A custom-designed fiber-optic cannula was mounted and secured on the skull using light-cured dental cement (Kuraray Inc.), with the optical fiber extending from the cannula's base to the desired depth (0.1 mm above the injection site). Following surgery, mice were kept on a heating pad until recovery from anesthesia and were given carprofen (5 mg/kg, subcutaneously [s.c.]

daily for 2 days to minimize post-operative discomfort. All experiments were conducted at least 4 weeks following virus injection to ensure optimal ChR2 expression. Probe locations were validated in all animals used for ofMRI experiments with T2-weighted structural MRI images.

### **Histology and immunohistochemistry to validate expression of ChR2**

To confirm the precise targeting of ChR2 to L2/3, L4, L5 or L6, a cohort of mice injected with the DIO-recombinant virus was deeply anesthetized with pentobarbital and transcardially perfused with 0.1 M PBS followed by ice-cold 4% paraformaldehyde (PFA) in PBS. Brains were extracted and fixed in 4 % PFA overnight at 4 °C. The brains were equilibrated in 20 % sucrose in PBS at 4 °C overnight. Axial sections of 50 µm thickness were prepared on a freezing microtome (Micron HM550 Microtome, Thermo Scientific Inc.). For immunohistochemistry, free floating sections were washed with 0.1 M PBS for 20 mins at room temperature. Sections were then exposed to 200 ng/ml of DAPI in PBS at room temperature for 20 mins. Slices were then washed and mounted using Fluoromount-G (SouthernBiotech, Birmingham, AL). Immuno-fluorescence was assessed with a laser confocal microscope (LSM 880 inverted confocal with Airyscan, Zeiss Inc.) at the Cell Sciences Imaging Facility at Beckman Center for Molecular and Genetics Medicine. The images were then analyzed to validate the expression of ChR2. Since the primary motor cortex is 1000 µm thick, and since the AAV5 spread is roughly 500 µm, region of interest (Figure 1A) was defined as a 500 µm × 1000 µm (width × height) rectangular box centered at the injection site. Anatomical landmarks including the midline, corpus callosum, cortex and striatum were identified and the ROI was defined based on the mouse brain atlas and injection site location to ensure consistency. For sensitivity, 12%, 15%, 23% and 15% of cells identified within the injection area were ChR2-EYFP-positive for *Drd3-Cre* (L2/3), *Scnn1-Cre* (L4), *Rpb4-Cre* (L5), or *Ntsr1-Cre* (L6) mouse lines, respectively. All mouse lines have 100% specificity.

### **ofMRI Experiments**

All MRI experiments were carried out on a 7 Tesla Bruker-converted Biospec small animal MRI system at the SCI3 facility at Clark Center using a transmit-only birdcage coil in combination with a custom-designed actively decoupled receive-only surface coil. Animals were initially anesthetized in an induction chamber with 5% isoflurane before placement into the restraining apparatus. The restrained animal was then placed onto the MRI-compatible cradle with ears, teeth, and head secured. To maximize signal-to-noise ratio, the receiver coil was first placed on top of the head and centered over the brain and then placed into the iso-center of the magnet. The animals were lightly anesthetized and sedated using a combination of isoflurane and dexmedetomidine (0.25% isoflurane mixed with O<sub>2</sub> and medical air; an initial bolus of 0.1 mg/kg dexmedetomidine; continuous infusion at 0.1 mg/kg/hr during scanning). During all fMRI experiments, continuous physiological monitoring was performed using an MRI-compatible system (SA Instruments). Vital signs were within normal physiological ranges (rectal temperature: 36.5 – 37.5 °C, heart rate: 260 – 420 beat/min, breathing: 80 – 120 breath/min, oxygen saturation: > 90%) throughout the duration of the experiments.

Fourteen contiguous 1.0-mm slices were positioned in the transverse orientation according to the mouse brain atlas to cover the whole brain. T2-weighted high-resolution anatomical images were acquired prior to fMRI to check for brain damage and confirm accurate probe location. These anatomical images were acquired using a rapid acquisition with relaxation enhancement (RARE) sequence with field of view (FOV) =  $20 \times 20 \text{ mm}^2$ , matrix =  $256 \times 256$ , RARE factor = 8, echo time (TE) = 33 ms, repetition time (TR) = 4,000 ms. ofMRI measurements were obtained for the same slices using a single-shot Gradient-Echo Echo-Planar-Imaging (GE-EPI) sequence with FOV =  $20 \times 20 \text{ mm}^2$ , matrix =  $75 \times 75$ , flip angle =  $40^\circ$ , TE = 14 ms, TR = 1,000 ms.

The MRI scanner and laser for optogenetic stimulation were synchronized using a Master pulse stimulator system (A.M.P.I.). The light delivery system was kept outside the magnet and long optical cables (~5 m) were used to deliver light into the scanner bore. Blue light was delivered using a 473-nm DPSS laser measured before scanning as 3 mW at the fiber tip (250  $\mu\text{m}$ ) corresponding to a light intensity of 60 mW/mm<sup>2</sup> for optogenetic stimulation. To determine the frequency-dependent spatiotemporal characteristics of evoked M1 layer-specific responses, four frequencies were used (5 Hz, 10 Hz, 20 Hz, and 40 Hz with 30% duty cycle). M1 layer-specific neurons were stimulated with a standard block design paradigm that consisted of 10-s light-on and 30-s light-off periods. Three to four trials were recorded for each frequency in a pseudo-random manner in each animal.

### **fMRI Data Analysis**

For each animal, all fMRI images were corrected for slice timing differences, realigned to the first image of the first fMRI session, and spatially smoothed with a Gaussian kernel (FWHM = 2 pixels) using SPM12 (Wellcome Department of Imaging Neuroscience, University College, London). The fMRI data were then temporally linear detrended and temporally band-pass filtered (0.01-0.25 Hz) to eliminate baseline drift caused by system instability and physiological noise. For detrending, linear trend was first calculated using linear regression of the global temporal signal obtained from the whole brain. Then, detrending was applied to the temporal signal of each voxel using the obtained linear trend. T2-weighted images from each animal were registered to a custom-made brain template acquired with the same settings. Registration was performed by affine transformation and Gaussian smoothing to maximize normalized mutual information (SPM12). Only then were the fMRI images resliced correspondingly.

A general linear model (GLM) was applied. Student's t test was performed to identify activated voxels using the threshold  $p < 0.001$ . The mapped responses were then compared between each animal to assess result quality before group level analysis. At the group level, realigned, registered, and resliced images corresponding to the same fMRI session were averaged across all animals. To quantify the activations from the activation maps, t-values within the ROI were extracted and averaged, while fraction of ROI positively and negatively modulated were calculated with a voxel-wise threshold of  $p < 0.05$  as positively or negatively modulated. BOLD temporal profiles for each stimulation frequency were extracted from identical ROIs delineated from the mouse brain atlas by regional averaging across the whole ROI.

Area under the curve of the BOLD profiles was calculated to quantify the strength of the BOLD responses for each individual animal, and then averaged across animals within the same group.

## **In Vivo Electrophysiology**

*In vivo* electrophysiology was performed to directly measure the neuronal activity of the ipsilateral M1, CPu and VL. Similar to fMRI experiments, the animals were lightly anesthetized and sedated using a combination of isoflurane and dexmedetomidine (0.25% isoflurane mixed with O<sub>2</sub> and medical air; an initial bolus of 0.1 mg/kg dexmedetomidine; continuous infusion at 0.1 mg/kg/hr during experiment). Throughout the procedure, body temperature was maintained at 37 °C using a thermoresistive heating pad (FHC, Inc., ME, USA). After securing the animal within a stereotactic frame, an optrode composed of an optical fiber glued to the 16-channel linear-array electrode (NeuroNexus Technologies, MI, USA; A1x16-5mm-150-703-A16 electrode array) was inserted at the stimulation site (+ 0.75 mm AP [anterior-posterior], - 1.5 mm ML [medial-lateral], covering between +0.00 mm and +2.40 mm DV [dorsal-ventral]) and a 16-channel microelectrode array (NeuroNexus Technologies, MI, USA; A1x16-5mm-50-703-A16 electrode array) was inserted at the ipsilateral VL (-1.35 mm AP, +1.00 mm ML, covering between +3.30 mm and +3.70 mm DV). Identical optogenetic stimulation paradigms were applied. Recordings were acquired at 40 kHz sampling rate using the Plexon OmniPlex system with PlexControl software (Plexon Inc., TX, USA). The Plexon multichannel acquisition processor was used to amplify and low-pass filter (cutoff frequency: 200 Hz) the acquired signal for local field potential (LFP) recordings or high-pass filter (cutoff frequency: 300 Hz) for spike recordings.

## **Electrophysiology Data Analysis**

For LFP recordings, raw data were initially imported into custom-written Matlab software and a notch filter centered at 60 Hz was applied to remove power-line noise. Individual animal LFPs were averaged across stimulation blocks to generate a single LFP trace for each stimulation frequency, which was then averaged across animals. For spike recordings, two-tailed paired t-tests were used to identify significant changes in firing rate within each unit between pre-stimulation and stimulation periods (10 seconds each). Only units with significant change (either increase or decrease) were included in the following analysis. Peri-event time histograms were averaged across stimulation blocks and units to generate an average peri-event time histograms for each stimulation frequency. One-way ANOVA followed by Bonferroni's post hoc test was applied to compare pre-stimulation, stimulation and post stimulation periods.

Although BOLD-fMRI and LFP responses reflects the overall signal within a region, which all recorded units should be considered when exploring the association between spiking, BOLD-fMRI and LFP, we still examined different spiking parameters namely percentage of positively modulated neurons, percentage of negatively modulated neurons, percentage of modulated neurons, average percentage spike rate change of positively modulated neurons,, average percentage spike rate change of negatively modulated neurons, average percentage spike rate change of all modulated neurons, average absolute value of

percentage spike rate change of all modulated neurons, average percentage spike rate change of all neurons, average absolute value of percentage spike rate change of all neurons, total percentage spike rate change of positively modulated neurons, total percentage spike rate change of negatively modulated neurons, total percentage spike rate change of all modulated neuron, total absolute value of percentage spike rate change of all modulated neurons, total percentage spike rate change of all neurons, and total absolute value of percentage spike rate change of all neurons. The summary of the  $R^2$  values of the scatter plots between these spiking parameters and brain-wide BOLD-fMRI (Supplementary Table 7), between these spiking parameters and long-range LFP recordings (Supplementary Table 8), between these spiking parameters and laminar BOLD-fMRI (Supplementary Table 9), and between these spiking parameters and laminar LFP recordings (Supplementary Table 10) generally showed that the spiking parameter, total absolute value of percentage spike rate change of all neurons, tends to yield the highest correlation.

## **Declarations**

## **AUTHOR CONTRIBUTIONS**

RWC participated in planning the study, performed surgeries, fMRI experiments, electrophysiological recordings, immunohistochemistry, data analysis, and wrote the paper. MA, HJL, and BE helped with electrode design, and electrophysiological recordings. HA and DF participated in the original planning of the study and provided the transgenic mouse lines. JHL planned the study, advised all personnel involved in the study, and wrote the paper.

## **ACKNOWLEDGEMENTS**

This work was supported by NIH/NIMH R01MH111444, and NIH/NIMH RF1MH11422701. The authors thank the entire Lee Lab for comments and help with the experiments.

## **DECLARATION OF INTERESTS**

HJL is an employee and shareholder of LVIS. JHL is a founder, shareholder, and consultant for LVIS.

## **DATA AND CODE AVAILABILITY**

Requests for raw data should be directed to and will be fulfilled by the Lead Contact, Jin Hyung Lee ([ljinhy@stanford.edu](mailto:ljinhy@stanford.edu)), Stanford University.

## **References**

1. Ebbsen, C. L. & Brecht, M. Motor cortex - to act or not to act? *Nature reviews. Neuroscience* **18**, 694–705, doi:10.1038/nrn.2017.119 (2017).
2. Weiler, N., Wood, L., Yu, J., Solla, S. A. & Shepherd, G. M. Top-down laminar organization of the excitatory network in motor cortex. *Nature neuroscience* **11**, 360–366, doi:10.1038/nn2049 (2008).
3. Gerfen, C. R., Economo, M. N. & Chandrashekar, J. Long distance projections of cortical pyramidal neurons. *Journal of neuroscience research* **96**, 1467–1475, doi:10.1002/jnr.23978 (2018).
4. Anderson, C. T., Sheets, P. L., Kiritani, T. & Shepherd, G. M. Sublayer-specific microcircuits of corticospinal and corticostriatal neurons in motor cortex. *Nature neuroscience* **13**, 739–744, doi:10.1038/nn.2538 (2010).
5. Yamawaki, N., Borges, K., Suter, B. A., Harris, K. D. & Shepherd, G. M. A genuine layer 4 in motor cortex with prototypical synaptic circuit connectivity. *eLife* **3**, e05422, doi:10.7554/eLife.05422 (2014).
6. Daigle, T. L. *et al.* A Suite of Transgenic Driver and Reporter Mouse Lines with Enhanced Brain-Cell-Type Targeting and Functionality. *Cell* **174**, 465–480 e422, doi:10.1016/j.cell.2018.06.035 (2018).
7. Boyden, E. S., Zhang, F., Bamberg, E., Nagel, G. & Deisseroth, K. Millisecond-timescale, genetically targeted optical control of neural activity. *Nature neuroscience* **8**, 1263–1268, doi:10.1038/nn1525 (2005).
8. Pluta, S. R., Telian, G. I., Naka, A. & Adesnik, H. Superficial layers suppress the deep layers to fine tune cortical coding. *The Journal of neuroscience: the official journal of the Society for Neuroscience*, doi:10.1523/JNEUROSCI.1459-18.2018 (2019).
9. Pluta, S. *et al.* A direct translaminar inhibitory circuit tunes cortical output. *Nature neuroscience* **18**, 1631–1640, doi:10.1038/nn.4123 (2015).
10. Bortone, D. S., Olsen, S. R. & Scanziani, M. Translaminar inhibitory cells recruited by layer 6 corticothalamic neurons suppress visual cortex. *Neuron* **82**, 474–485, doi:10.1016/j.neuron.2014.02.021 (2014).
11. Kim, J., Matney, C. J., Blankenship, A., Hestrin, S. & Brown, S. P. Layer 6 corticothalamic neurons activate a cortical output layer, layer 5a. *The Journal of neuroscience: the official journal of the Society for Neuroscience* **34**, 9656–9664, doi:10.1523/JNEUROSCI.1325-14.2014 (2014).
12. Xiong, X. R. *et al.* Auditory cortex controls sound-driven innate defense behaviour through corticofugal projections to inferior colliculus. *Nature communications* **6**, 7224, doi:10.1038/ncomms8224 (2015).
13. Liang, F. *et al.* Sensory Cortical Control of a Visually Induced Arrest Behavior via Corticotectal Projections. *Neuron* **86**, 755–767, doi:10.1016/j.neuron.2015.03.048 (2015).
14. Huber, L. *et al.* High-Resolution CBV-fMRI Allows Mapping of Laminar Activity and Connectivity of Cortical Input and Output in Human M1. *Neuron* **96**, 1253–1263 e1257, doi:10.1016/j.neuron.2017.11.005 (2017).
15. Lawrence, S. J. D., Formisano, E., Muckli, L. & de Lange, F. P. Laminar fMRI: Applications for cognitive neuroscience. *NeuroImage* **197**, 785–791, doi:10.1016/j.neuroimage.2017.07.004 (2019).

16. Stephan, K. E. *et al.* Laminar fMRI and computational theories of brain function. *NeuroImage* **197**, 699–706, doi:10.1016/j.neuroimage.2017.11.001 (2019).
17. Lee, J. H. *et al.* Global and local fMRI signals driven by neurons defined optogenetically by type and wiring. *Nature* **465**, 788–792, doi:10.1038/nature09108 (2010).
18. Liu, J. *et al.* Frequency-selective control of cortical and subcortical networks by central thalamus. *eLife* **4**, e09215, doi:10.7554/eLife.09215 (2015).
19. Lee, J. H., Kreitzer, A. C., Singer, A. C. & Schiff, N. D. Illuminating Neural Circuits: From Molecules to MRI. *The Journal of neuroscience: the official journal of the Society for Neuroscience* **37**, 10817–10825, doi:10.1523/JNEUROSCI.2569-17.2017 (2017).
20. Duffy, B. A., Choy, M., Chuapoco, M. R., Madsen, M. & Lee, J. H. MRI compatible optrodes for simultaneous LFP and optogenetic fMRI investigation of seizure-like afterdischarges. *NeuroImage* **123**, 173–184, doi:10.1016/j.neuroimage.2015.07.038 (2015).
21. Weitz, A. J. *et al.* Optogenetic fMRI reveals distinct, frequency-dependent networks recruited by dorsal and intermediate hippocampus stimulations. *NeuroImage* **107**, 229–241, doi:10.1016/j.neuroimage.2014.10.039 (2015).
22. Chan, R. W. *et al.* Low-frequency hippocampal-cortical activity drives brain-wide resting-state functional MRI connectivity. *Proceedings of the National Academy of Sciences of the United States of America* **114**, E6972–E6981, doi:10.1073/pnas.1703309114 (2017).
23. Gong, S. *et al.* Targeting Cre recombinase to specific neuron populations with bacterial artificial chromosome constructs. *The Journal of neuroscience: the official journal of the Society for Neuroscience* **27**, 9817–9823, doi:10.1523/JNEUROSCI.2707-07.2007 (2007).
24. Madisen, L. *et al.* A robust and high-throughput Cre reporting and characterization system for the whole mouse brain. *Nature neuroscience* **13**, 133–140, doi:10.1038/nn.2467 (2010).
25. Adesnik, H. & Scanziani, M. Lateral competition for cortical space by layer-specific horizontal circuits. *Nature* **464**, 1155–1160, doi:10.1038/nature08935 (2010).
26. Weitz, A. J., Lee, H. J., Choy, M. & Lee, J. H. Thalamic Input to Orbitofrontal Cortex Drives Brain-wide, Frequency-Dependent Inhibition Mediated by GABA and Zona Incerta. *Neuron* **104**, 1153–1167 e1154, doi:10.1016/j.neuron.2019.09.023 (2019).
27. Christie, I. N. *et al.* fMRI response to blue light delivery in the naive brain: implications for combined optogenetic fMRI studies. *NeuroImage* **66**, 634–641, doi:10.1016/j.neuroimage.2012.10.074 (2013).
28. Schmid, F. *et al.* True and apparent optogenetic BOLD fMRI signals. *Magnetic resonance in medicine* **77**, 126–136, doi:10.1002/mrm.26095 (2017).
29. Kozai, T. D. & Vazquez, A. L. Photoelectric artefact from optogenetics and imaging on microelectrodes and bioelectronics: New Challenges and Opportunities. *Journal of materials chemistry. B* **3**, 4965–4978, doi:10.1039/C5TB00108K (2015).
30. Mikulovic, S. *et al.* On the photovoltaic effect in local field potential recordings. *Neurophotonics* **3**, 015002, doi:10.1117/1.NPh.3.1.015002 (2016).

31. Brodmann, K. Brodmann's Localisation in the Cerebral Cortex Translated from German by Laurence J Garey. *Imperial College Press* (1909).
32. Bastos, A. M. *et al.* Canonical microcircuits for predictive coding. *Neuron* **76**, 695–711, doi:10.1016/j.neuron.2012.10.038 (2012).
33. Krieg, W. J. Connections of the cerebral cortex; the albino rat; structure of the cortical areas. *The Journal of comparative neurology* **84**, 277–323, doi:10.1002/cne.900840302 (1946).
34. Garcia-Cabezas, M. A. & Barbas, H. Area 4 has layer IV in adult primates. *The European journal of neuroscience* **39**, 1824–1834, doi:10.1111/ejn.12585 (2014).
35. Strick, P. L. & Sterling, P. Synaptic termination of afferents from the ventrolateral nucleus of the thalamus in the cat motor cortex. A light and electron microscopy study. *The Journal of comparative neurology* **153**, 77–106, doi:10.1002/cne.901530107 (1974).
36. Kuramoto, E. *et al.* Two types of thalamocortical projections from the motor thalamic nuclei of the rat: a single neuron-tracing study using viral vectors. *Cerebral cortex* **19**, 2065–2077, doi:10.1093/cercor/bhn231 (2009).
37. Bopp, R., Holler-Rickauer, S., Martin, K. A. & Schuhknecht, G. F. An Ultrastructural Study of the Thalamic Input to Layer 4 of Primary Motor and Primary Somatosensory Cortex in the Mouse. *The Journal of neuroscience: the official journal of the Society for Neuroscience* **37**, 2435–2448, doi:10.1523/JNEUROSCI.2557-16.2017 (2017).
38. Poewe, W. *et al.* Parkinson disease. *Nature reviews. Disease primers* **3**, 17013, doi:10.1038/nrdp.2017.13 (2017).
39. Fearnley, J. M. & Lees, A. J. Ageing and Parkinson's disease: substantia nigra regional selectivity. *Brain: a journal of neurology* **114 (Pt 5)**, 2283–2301, doi:10.1093/brain/114.5.2283 (1991).
40. Damier, P., Hirsch, E. C., Agid, Y. & Graybiel, A. M. The substantia nigra of the human brain. II. Patterns of loss of dopamine-containing neurons in Parkinson's disease. *Brain: a journal of neurology* **122 (Pt 8)**, 1437–1448, doi:10.1093/brain/122.8.1437 (1999).
41. Lindenbach, D. & Bishop, C. Critical involvement of the motor cortex in the pathophysiology and treatment of Parkinson's disease. *Neuroscience and biobehavioral reviews* **37**, 2737–2750, doi:10.1016/j.neubiorev.2013.09.008 (2013).
42. Guo, L. *et al.* Dynamic rewiring of neural circuits in the motor cortex in mouse models of Parkinson's disease. *Nature neuroscience* **18**, 1299–1309, doi:10.1038/nn.4082 (2015).
43. Burciu, R. G. & Vaillancourt, D. E. Imaging of Motor Cortex Physiology in Parkinson's Disease. *Movement disorders: official journal of the Movement Disorder Society* **33**, 1688–1699, doi:10.1002/mds.102 (2018).
44. Gaspar, P., Duyckaerts, C., Alvarez, C., Javoy-Agid, F. & Berger, B. Alterations of dopaminergic and noradrenergic innervations in motor cortex in Parkinson's disease. *Annals of neurology* **30**, 365–374, doi:10.1002/ana.410300308 (1991).
45. Limousin, P. *et al.* Electrical stimulation of the subthalamic nucleus in advanced Parkinson's disease. *The New England journal of medicine* **339**, 1105–1111, doi:10.1056/NEJM199810153391603

(1998).

46. Fitzgerald, P. B., Fountain, S. & Daskalakis, Z. J. A comprehensive review of the effects of rTMS on motor cortical excitability and inhibition. *Clinical neurophysiology: official journal of the International Federation of Clinical Neurophysiology* **117**, 2584–2596, doi:10.1016/j.clinph.2006.06.712 (2006).
47. Wu, A. D., Fregni, F., Simon, D. K., Deblieck, C. & Pascual-Leone, A. Noninvasive brain stimulation for Parkinson's disease and dystonia. *Neurotherapeutics: the journal of the American Society for Experimental NeuroTherapeutics* **5**, 345–361, doi:10.1016/j.nurt.2008.02.002 (2008).
48. Elahi, B., Elahi, B. & Chen, R. Effect of transcranial magnetic stimulation on Parkinson motor function—systematic review of controlled clinical trials. *Movement disorders: official journal of the Movement Disorder Society* **24**, 357–363, doi:10.1002/mds.22364 (2009).
49. Fregni, F., Simon, D. K., Wu, A. & Pascual-Leone, A. Non-invasive brain stimulation for Parkinson's disease: a systematic review and meta-analysis of the literature. *Journal of neurology, neurosurgery, and psychiatry* **76**, 1614–1623, doi:10.1136/jnnp.2005.069849 (2005).
50. Cenci, M. A., Ohlin, K. E. & Odin, P. Current options and future possibilities for the treatment of dyskinesia and motor fluctuations in Parkinson's disease. *CNS & neurological disorders drug targets* **10**, 670–684 (2011).
51. Gradinaru, V., Mogri, M., Thompson, K. R., Henderson, J. M. & Deisseroth, K. Optical deconstruction of parkinsonian neural circuitry. *Science* **324**, 354–359, doi:10.1126/science.1167093 (2009).
52. Carroll, D. *et al.* Motor cortex stimulation for chronic neuropathic pain: a preliminary study of 10 cases. *Pain* **84**, 431–437, doi:10.1016/s0304-3959(99)00245-6 (2000).
53. Rasche, D., Ruppolt, M., Stippich, C., Unterberg, A. & Tronnier, V. M. Motor cortex stimulation for long-term relief of chronic neuropathic pain: a 10 year experience. *Pain* **121**, 43–52, doi:10.1016/j.pain.2005.12.006 (2006).
54. Lefaucheur, J. P., Drouot, X., Menard-Lefaucheur, I., Keravel, Y. & Nguyen, J. P. Motor cortex rTMS restores defective intracortical inhibition in chronic neuropathic pain. *Neurology* **67**, 1568–1574, doi:10.1212/01.wnl.0000242731.10074.3c (2006).
55. Nouri, S. & Cramer, S. C. Anatomy and physiology predict response to motor cortex stimulation after stroke. *Neurology* **77**, 1076–1083, doi:10.1212/WNL.0b013e31822e1482 (2011).
56. Schlaug, G., Renga, V. & Nair, D. Transcranial direct current stimulation in stroke recovery. *Archives of neurology* **65**, 1571–1576, doi:10.1001/archneur.65.12.1571 (2008).
57. Brown, J. A., Lutsep, H. L., Weinand, M. & Cramer, S. C. Motor cortex stimulation for the enhancement of recovery from stroke: a prospective, multicenter safety study. *Neurosurgery* **58**, 464–473, doi:10.1227/01.NEU.0000197100.63931.04 (2006).
58. Bullmore, E. & Sporns, O. Complex brain networks: graph theoretical analysis of structural and functional systems. *Nature reviews. Neuroscience* **10**, 186–198, doi:10.1038/nrn2575 (2009).
59. Eichenbaum, H. A cortical-hippocampal system for declarative memory. *Nature reviews. Neuroscience* **1**, 41–50, doi:10.1038/35036213 (2000).

60. Logothetis, N. K. What we can do and what we cannot do with fMRI. *Nature* **453**, 869–878, doi:10.1038/nature06976 (2008).
61. Uhlirova, H. *et al.* Cell type specificity of neurovascular coupling in cerebral cortex. *eLife* **5**, doi:10.7554/eLife.14315 (2016).
62. Berens, P., Logothetis, N. & Tolias, A. Local field potentials, BOLD and spiking activity – relationships and physiological mechanisms. *Nature Precedings*, doi:10.1038/npre.2010.5216.1 (2010).
63. Lee, H. J. *et al.* Activation of Direct and Indirect Pathway Medium Spiny Neurons Drives Distinct Brain-wide Responses. *Neuron* **91**, 412–424, doi:10.1016/j.neuron.2016.06.010 (2016).
64. Mishra, A. M. *et al.* Where fMRI and electrophysiology agree to disagree: corticothalamic and striatal activity patterns in the WAG/Rij rat. *The Journal of neuroscience: the official journal of the Society for Neuroscience* **31**, 15053–15064, doi:10.1523/JNEUROSCI.0101-11.2011 (2011).
65. Schridde, U. *et al.* Negative BOLD with large increases in neuronal activity. *Cerebral cortex* **18**, 1814–1827, doi:10.1093/cercor/bhm208 (2008).
66. Shih, Y. Y. *et al.* A new scenario for negative functional magnetic resonance imaging signals: endogenous neurotransmission. *The Journal of neuroscience: the official journal of the Society for Neuroscience* **29**, 3036–3044, doi:10.1523/JNEUROSCI.3447-08.2009 (2009).
67. Goense, J. B. & Logothetis, N. K. Laminar specificity in monkey V1 using high-resolution SE-fMRI. *Magnetic resonance imaging* **24**, 381–392, doi:10.1016/j.mri.2005.12.032 (2006).
68. Schmid, F., Tsai, P. S., Kleinfeld, D., Jenny, P. & Weber, B. Depth-dependent flow and pressure characteristics in cortical microvascular networks. *PLoS computational biology* **13**, e1005392, doi:10.1371/journal.pcbi.1005392 (2017).

## Figures

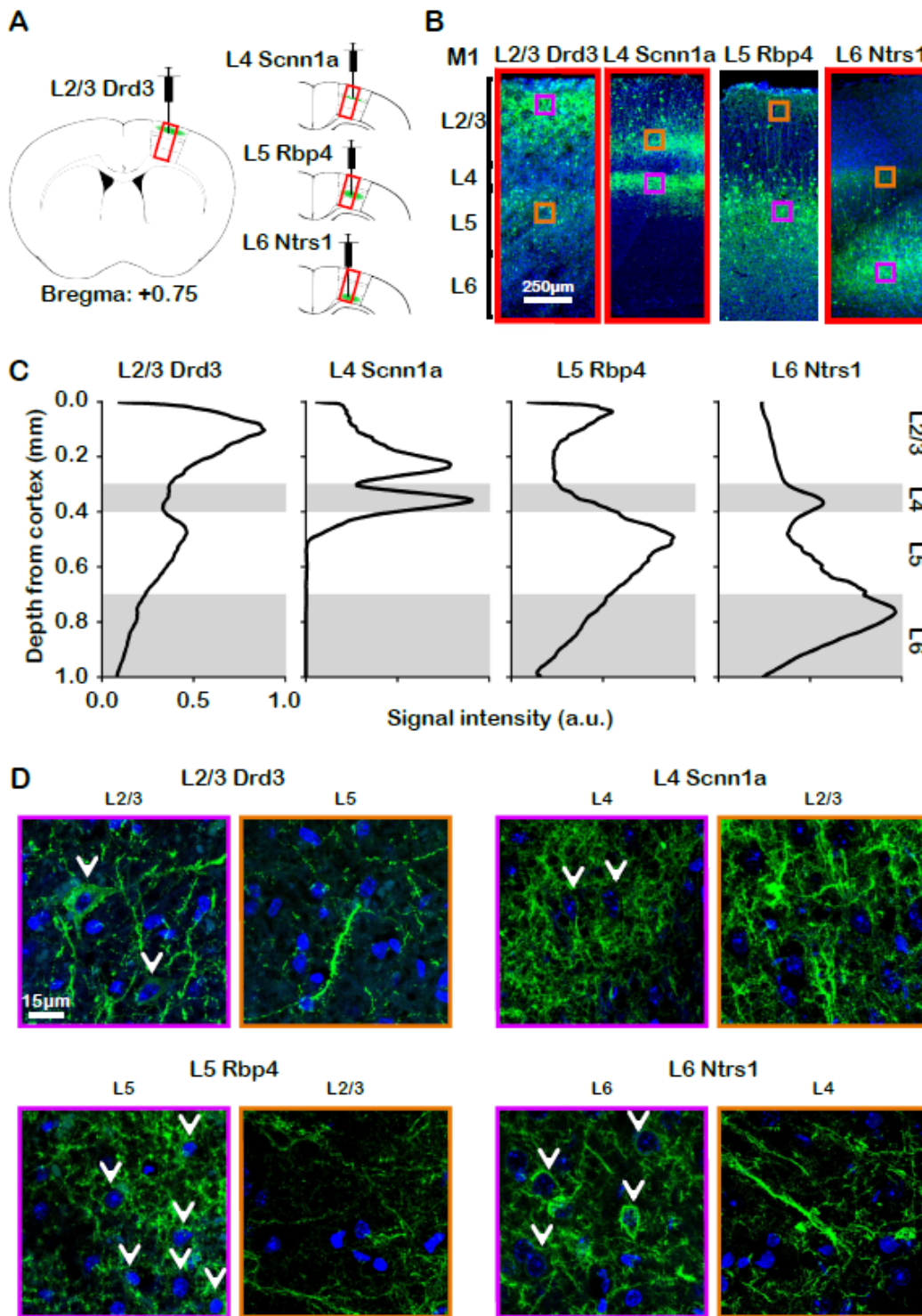


**Figure 1**

Histology reveals ChR2 expression of Drd3 L2/3, Scnn1a L4, Rbp4 L5 and Ntrs1 L6 Cre-line mice in their respective M1 layers and their projections. (A) Illustration presents the viral injection sites in respective layers of M1. (B) Representative fluorescence images from the four layer-specific Cre-lines show robust ChR2-EYFP expression throughout their respective layers and intra-cortical projections in the M1. (C) Normalized signal intensity plots along the M1 cortical depth show a local peak throughout their

respective layers and intra-cortical projections. (D) Merged representative confocal images of ChR2-EYFP and stained nuclear marker DAPI confirmed colocalization of ChR2-EYFP and M1 neurons throughout their respective layers (white arrows), but not their intra-cortical projections. Together, ChR2-EYFP expression is observed in L2/3 M1 neurons and L5 projections for *Drd3* L2/3 Cre-line, in L4 M1 neurons and L2/3 projections for *Scnn1a* L4 Cre-line, in L5 M1 neurons and L2/3 projections for *Rbp4* L5 Cre-line, and in L6 M1 neurons and L4 projections for *Ntrs1* L6 Cre-line.

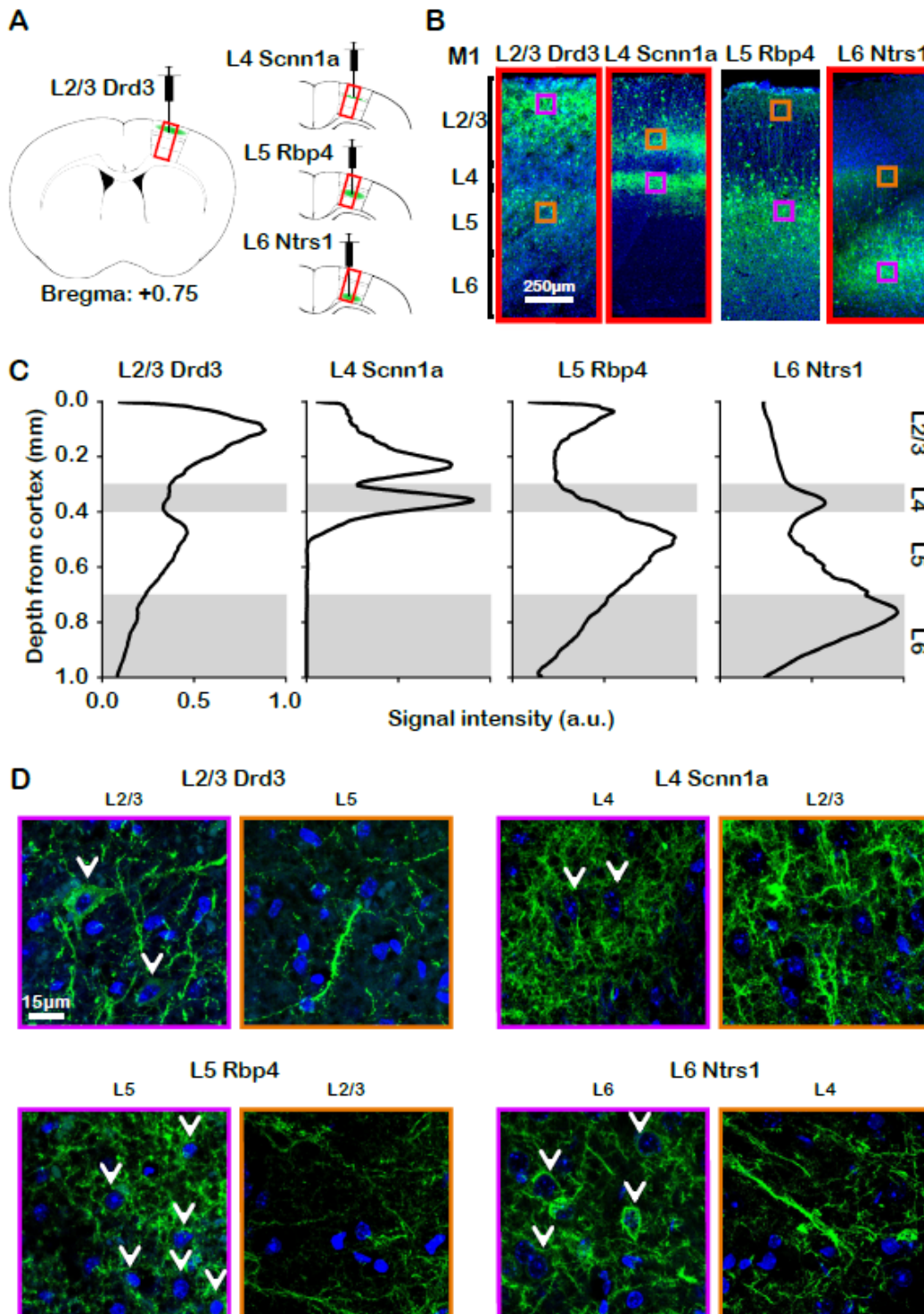
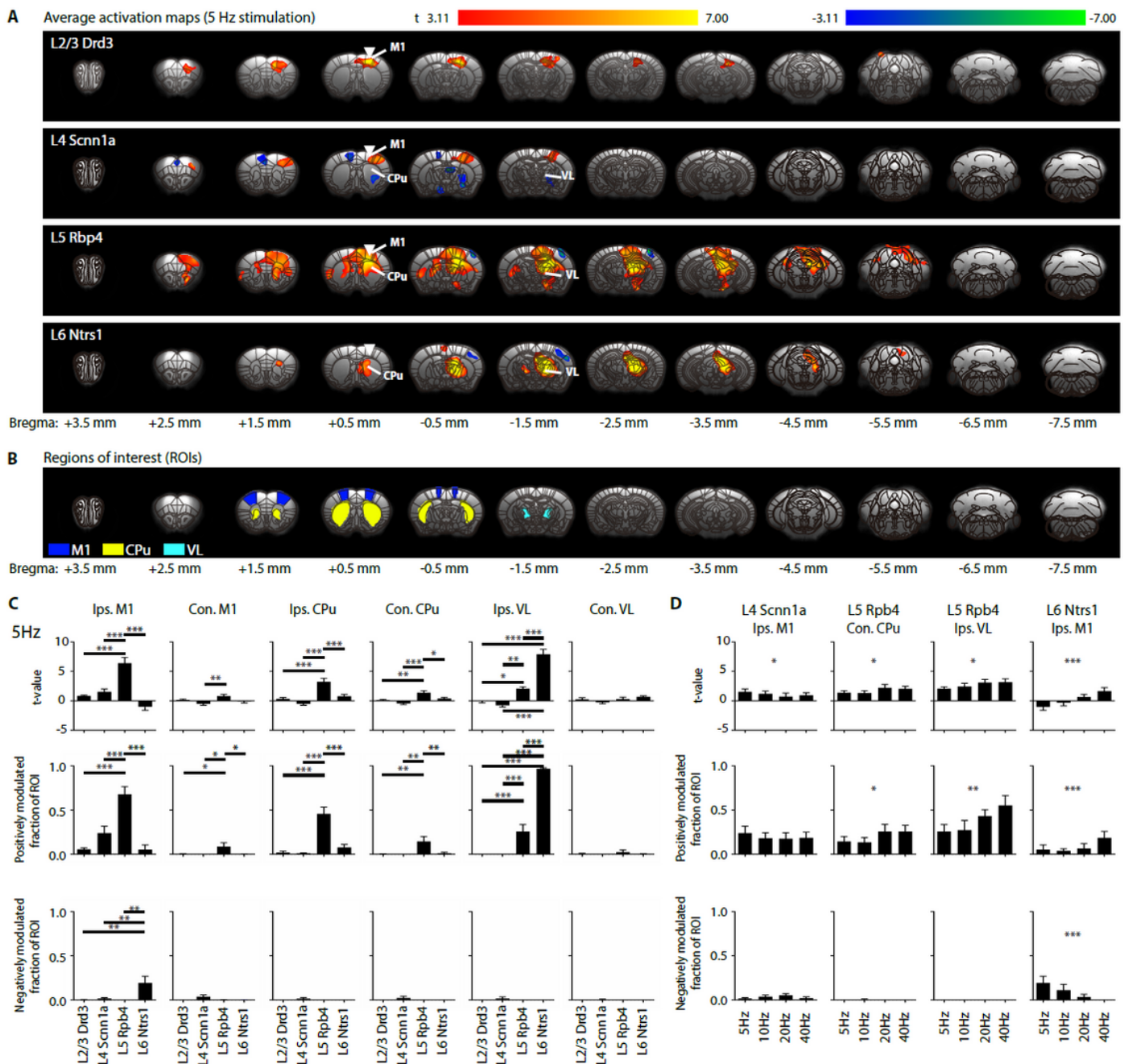


Figure 1

Histology reveals ChR2 expression of *Drd3* L2/3, *Scnn1a* L4, *Rbp4* L5 and *Ntrs1* L6 Cre-line mice in their respective M1 layers and their projections. (A) Illustration presents the viral injection sites in respective layers of M1. (B) Representative fluorescence images from the four layer-specific Cre-lines show robust ChR2-EYFP expression throughout their respective layers and intra-cortical projections in the M1. (C) Normalized signal intensity plots along the M1 cortical depth show a local peak throughout their respective layers and intra-cortical projections. (D) Merged representative confocal images of ChR2-EYFP and stained nuclear marker DAPI confirmed colocalization of ChR2-EYFP and M1 neurons throughout their respective layers (white arrows), but not their intra-cortical projections. Together, ChR2-EYFP expression is observed in L2/3 M1 neurons and L5 projections for *Drd3* L2/3 Cre-line, in L4 M1 neurons and L2/3 projections for *Scnn1a* L4 Cre-line, in L5 M1 neurons and L2/3 projections for *Rbp4* L5 Cre-line, and in L6 M1 neurons and L4 projections for *Ntrs1* L6 Cre-line.



## Figure 2

Layer-specific M1 stimulations evoked distinct brain-wide ofMRI responses. (A) Group-level activation maps during L2/3, L4, L5, and L6 M1 stimulation at 5 Hz (n = 12 animals per Cre-line, total N = 48 animals;  $p < 0.001$ , FDR-corrected). Inverted white triangle indicates site of stimulation; warm and cool colors indicate positive and negative t-scores, respectively. Abbreviations: primary motor cortex (M1), caudate putamen (CPu), ventrolateral thalamic nucleus (VL). (B) Regions of interest (ROIs) are defined based on the mouse brain atlas to quantify the activation maps. (C) Average t-values (top), fraction of ROI positively (middle) and negatively (bottom) modulated were extracted. L2/3 stimulation activated only ipsilateral M1. L4 stimulation activated ipsilateral M1, while small negative responses were observed in contralateral M1, ipsilateral CPu and ipsilateral VL. L5 stimulation evoked robust ipsilateral M1, bilateral CPu and ipsilateral VL activations. L6 stimulation evoked negative ipsilateral M1 response, positive ipsilateral CPu response and robust VL activations. L5 stimulation evoked the strongest responses in ipsilateral M1 and bilateral CPu compared to L2/3, L4 and L6 stimulations. For ipsilateral VL, L6 stimulation evoked the strongest activations, while L5 stimulation evoked stronger activations compared to L2/3 and L4 stimulations. One-way ANOVA followed by Bonferroni's post hoc test was used ( $*p < 0.05$ ,  $**p < 0.01$  and  $***p < 0.001$ ; error bars indicate  $\pm$ SEM). (D) Average t-values (top), fraction of ROI positively (middle) and negatively (bottom) modulated were extracted to compare ofMRI responses between different frequencies (5 Hz, 10 Hz, 20 Hz and 40 Hz). The extracted t-values had a decreasing trend with frequency in ipsilateral M1 during L4 stimulation, while both the extracted t-values and fraction of ROI positively modulated had an increasing trend with frequency in contralateral CPu and ipsilateral VL during L5 stimulation. For L6 stimulation, ipsilateral M1 responses had increasing trends with increasing stimulation frequency for t-values and fraction of ROI positively modulated, while a decreasing trend with frequency was observed for fraction of ROI negatively modulated. One-way ANOVA followed by trend analysis was applied ( $*p < 0.05$ ,  $**p < 0.01$  and  $***p < 0.001$ ; error bars indicate  $\pm$ SEM).

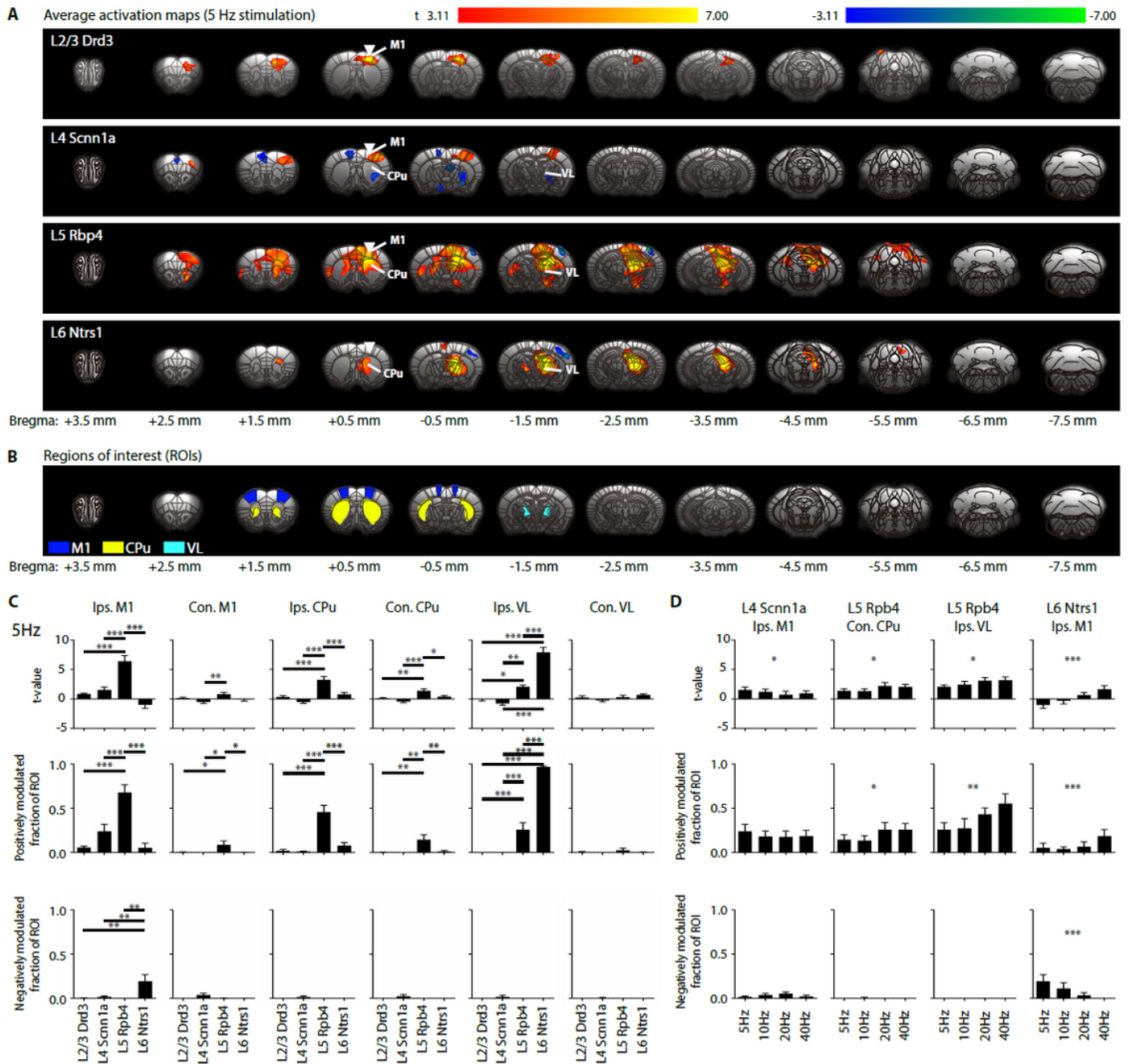


**Figure 2**

Layer-specific M1 stimulations evoked distinct brain-wide ofMRI responses. (A) Group-level activation maps during L2/3, L4, L5, and L6 M1 stimulation at 5 Hz ( $n = 12$  animals per Cre-line, total  $N = 48$  animals;  $p < 0.001$ , FDR-corrected). Inverted white triangle indicates site of stimulation; warm and cool colors indicate positive and negative t-scores, respectively. Abbreviations: primary motor cortex (M1), caudate putamen (CPu), ventrolateral thalamic nucleus (VL). (B) Regions of interest (ROIs) are defined based on the mouse brain atlas to quantify the activation maps. (C) Average t-values (top), fraction of ROI positively (middle) and negatively (bottom) modulated were extracted. L2/3 stimulation activated only ipsilateral M1. L4 stimulation activated ipsilateral M1, while small negative responses were observed in contralateral M1, ipsilateral CPu and ipsilateral VL. L5 stimulation evoked robust ipsilateral M1,

bilateral CPu and ipsilateral VL activations. L6 stimulation evoked negative ipsilateral M1 response, positive ipsilateral CPu response and robust VL activations. L5 stimulation evoked the strongest responses in ipsilateral M1 and bilateral CPu compared to L2/3, L4 and L6 stimulations. For ipsilateral VL, L6 stimulation evoked the strongest activations, while L5 stimulation evoked stronger activations compared to L2/3 and L4 stimulations. One-way ANOVA followed by Bonferroni's post hoc test was used (\*p < 0.05, \*\*p < 0.01 and \*\*\*p < 0.001; error bars indicate  $\pm$ SEM). (D) Average t-values (top), fraction of ROI positively (middle) and negatively (bottom) modulated were extracted to compare ofMRI responses between different frequencies (5 Hz, 10 Hz, 20 Hz and 40 Hz). The extracted t-values had a decreasing trend with frequency in ipsilateral M1 during L4 stimulation, while both the extracted t-values and fraction of ROI positively modulated had an increasing trend with frequency in contralateral CPu and ipsilateral VL during L5 stimulation. For L6 stimulation, ipsilateral M1 responses had increasing trends with increasing stimulation frequency for t-values and fraction of ROI positively modulated, while a decreasing trend with frequency was observed for fraction of ROI negatively modulated. One-way ANOVA followed by trend analysis was applied (\*p < 0.05, \*\*p < 0.01 and \*\*\*p < 0.001; error bars indicate  $\pm$ SEM).

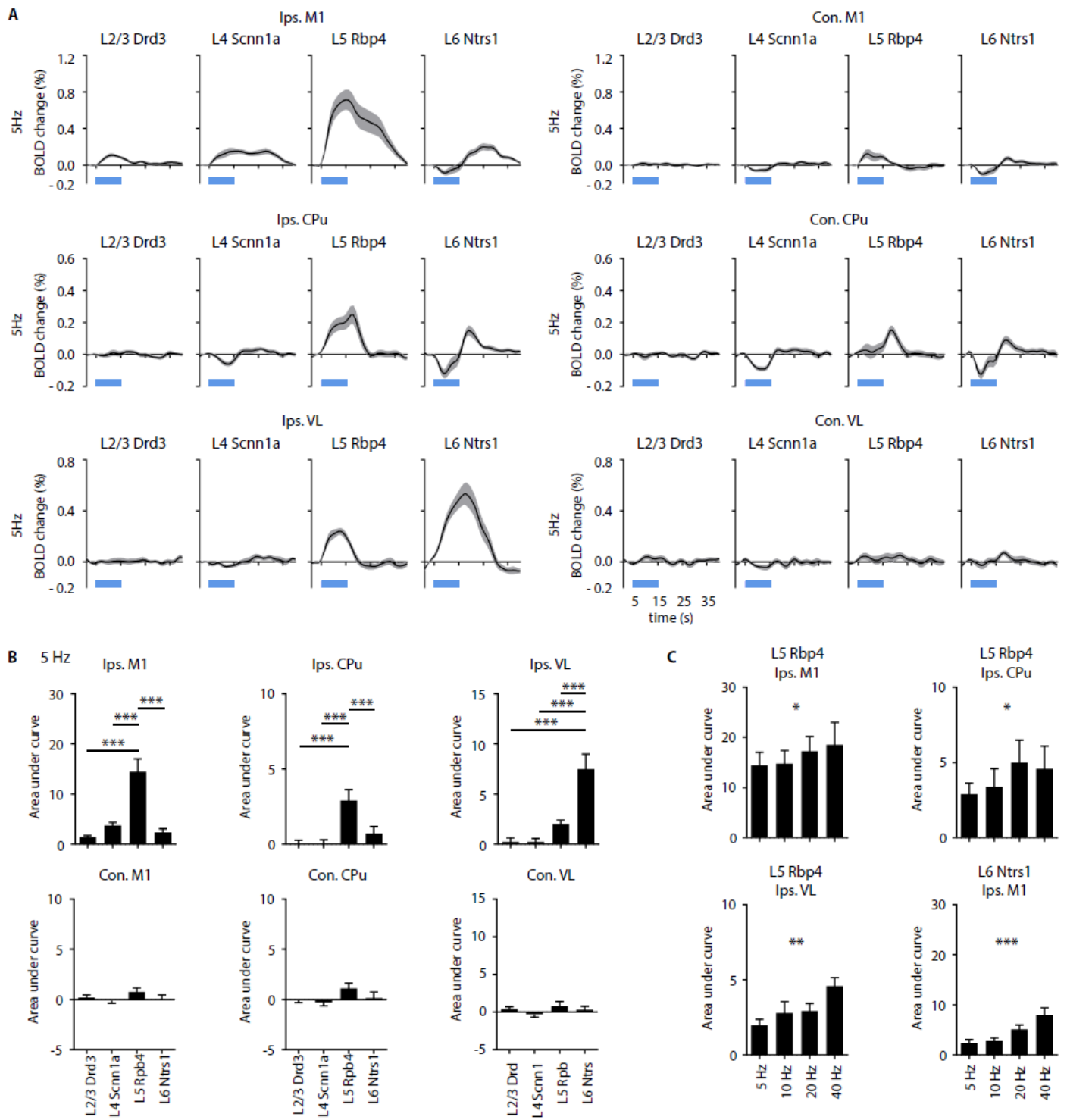


**Figure 3**

Distinct of MRI temporal dynamics of the BOLD signal across the brain evoked by layer-specific M1 stimulation. (A) BOLD signal profiles extracted from the same ROIs used for quantifying activation maps in Figure 2B. Abbreviations: primary motor cortex (M1), caudate putamen (CPU), ventrolateral thalamic nucleus (VL). (B) Area under the curve (AUC) was calculated for the comparison of the extracted BOLD signal. L5 stimulation evoked the strongest responses in ipsilateral M1 and ipsilateral CPU compared to

L2/3, L4 and L6 stimulations; while L6 stimulation evoked the strongest ipsilateral VL activations. These results were in line with Figure 2. One-way ANOVA followed by Bonferroni's post hoc test was used (n = 12 animals per Cre-line, total N = 48 animals; \*p < 0.05, \*\*p < 0.01 and \*\*\*p < 0.001; error bars indicate  $\pm$ SEM). (C) Similarly, AUC was calculated for the comparison of the extracted BOLD signal between different frequencies (5 Hz, 10 Hz, 20 Hz and 40 Hz). AUC had an increasing trend in ipsilateral M1 during L5 and L6 stimulations, as well as ipsilateral CPu and VL during L5 stimulation. One-way ANOVA followed by trend analysis was applied (\*p < 0.05, \*\*p < 0.01 and \*\*\*p < 0.001; error bars indicate  $\pm$ SEM).

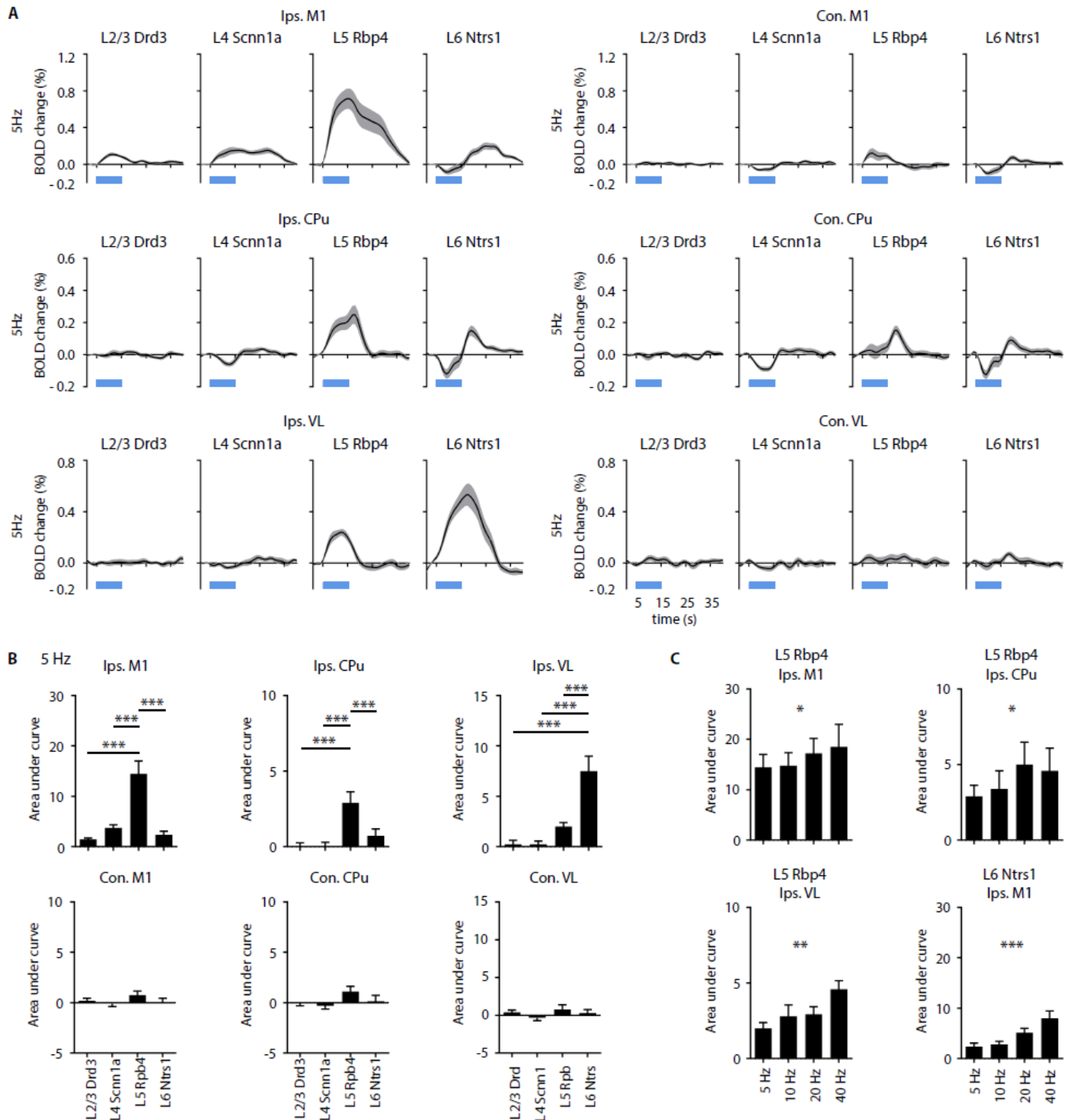


### Figure 3

Distinct ofMRI temporal dynamics of the BOLD signal across the brain evoked by layer-specific M1 stimulation. (A) BOLD signal profiles extracted from the same ROIs used for quantifying activation maps in Figure 2B. Abbreviations: primary motor cortex (M1), caudate putamen (CPu), ventrolateral thalamic nucleus (VL). (B) Area under the curve (AUC) was calculated for the comparison of the extracted BOLD signal. L5 stimulation evoked the strongest responses in ipsilateral M1 and ipsilateral CPu compared to L2/3, L4 and L6 stimulations; while L6 stimulation evoked the strongest ipsilateral VL activations. These results were in line with Figure 2. One-way ANOVA followed by Bonferroni's post hoc test was used (n = 12 animals per Cre-line, total N = 48 animals; \*p < 0.05, \*\*p < 0.01 and \*\*\*p < 0.001; error bars indicate  $\pm$ SEM). (C) Similarly, AUC was calculated for the comparison of the extracted BOLD signal between different frequencies (5 Hz, 10 Hz, 20 Hz and 40 Hz). AUC had an increasing trend in ipsilateral M1 during L5 and L6 stimulations, as well as ipsilateral CPu and VL during L5 stimulation. One-way ANOVA followed by trend analysis was applied (\*p < 0.05, \*\*p < 0.01 and \*\*\*p < 0.001; error bars indicate  $\pm$ SEM).

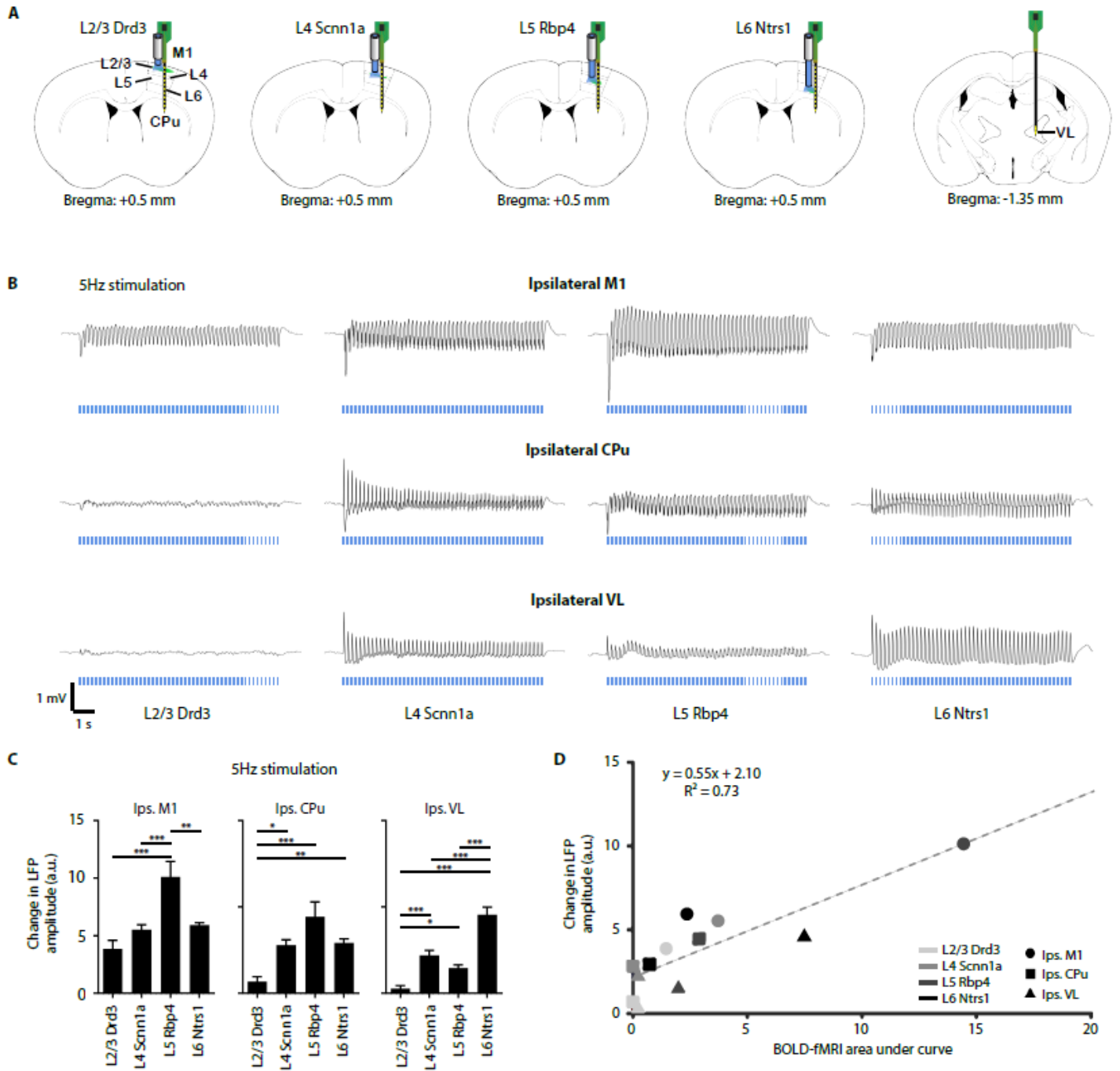


**Figure 4**

LFP recordings reveal activations in M1 for all layer-specific stimulations and in CPu and VL for L4, L5 and L6 stimulations only, which correlates with fMRI activations. (A) Schematic shows recording optrode and electrode locations in ipsilateral M1, CPu, and VL. (B) Average LFP (n = 4 animals per Cre-line, total N = 16 animals) from ipsilateral M1, VL, and CPu layer-specific M1 stimulation at 5 Hz shows robust activation in M1 for all Cre-lines, and in CPu and VL for Scnn1a L4, Rbp4 L5 and Ntrs1 L6 Cre-lines. (C) Change in LFP amplitude during stimulation was calculated to quantify the LFP traces. L5 stimulation evoked the strongest change in LFP amplitude in ipsilateral M1 compared to L2/3, L4 and L6

stimulations. L2/3 stimulation evoked the weakest change in LFP amplitude in ipsilateral CPu. For ipsilateral VL, L6 stimulation evoked the strongest change in LFP amplitude, while L5 and L4 stimulation evoked stronger activations compared to L2/3. These LFP results corroborate with our fMRI results. One-way ANOVA followed by Bonferroni's post hoc test was used (\* $p < 0.05$ , \*\* $p < 0.01$  and \*\*\* $p < 0.001$ ; error bars indicate  $\pm$ SEM). (D) Scatter plot shows correlation between change in LFP amplitude and BOLD-fMRI area under the curve in ipsilateral M1, CPu, and VL for all Cre-lines.

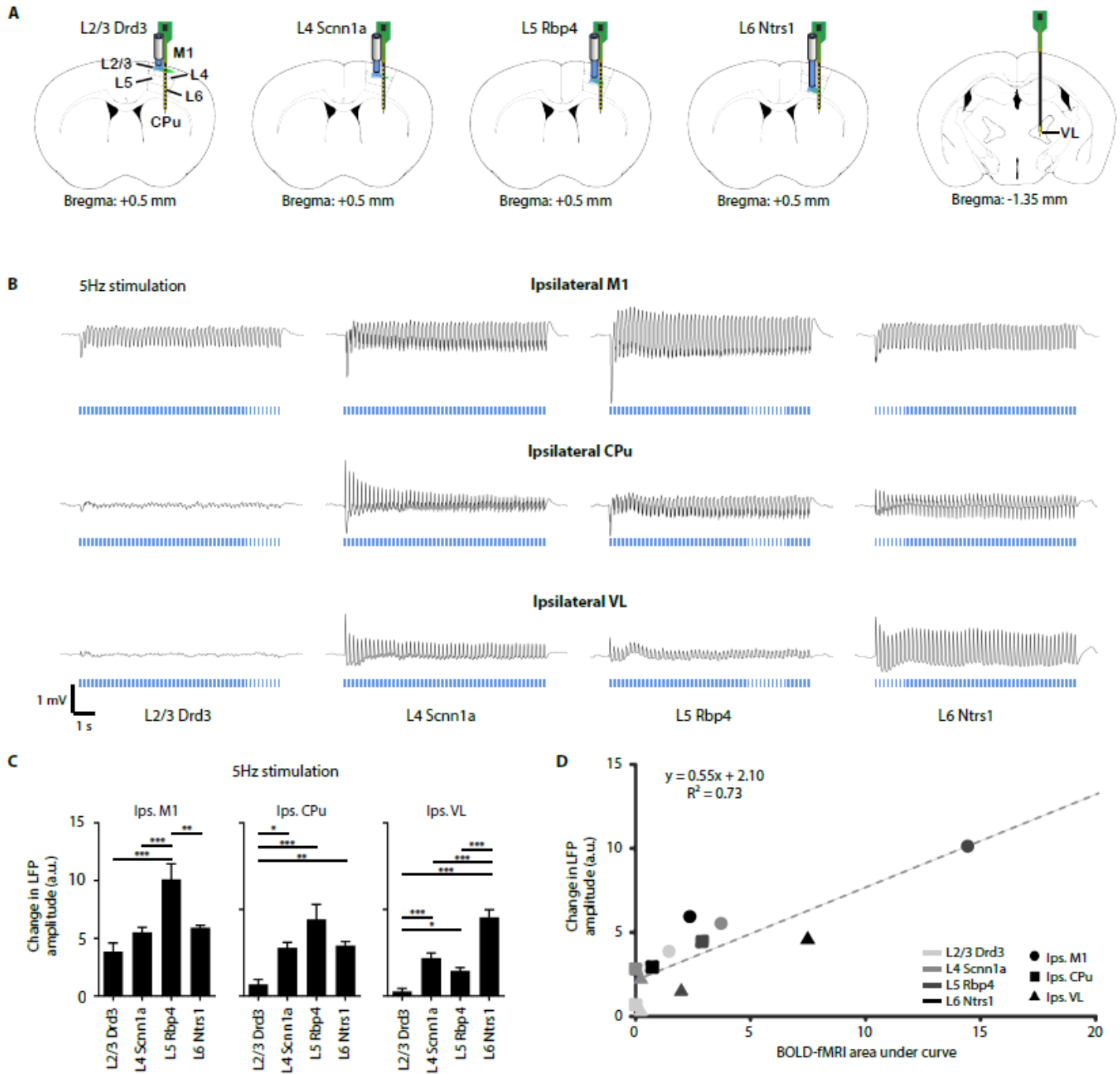
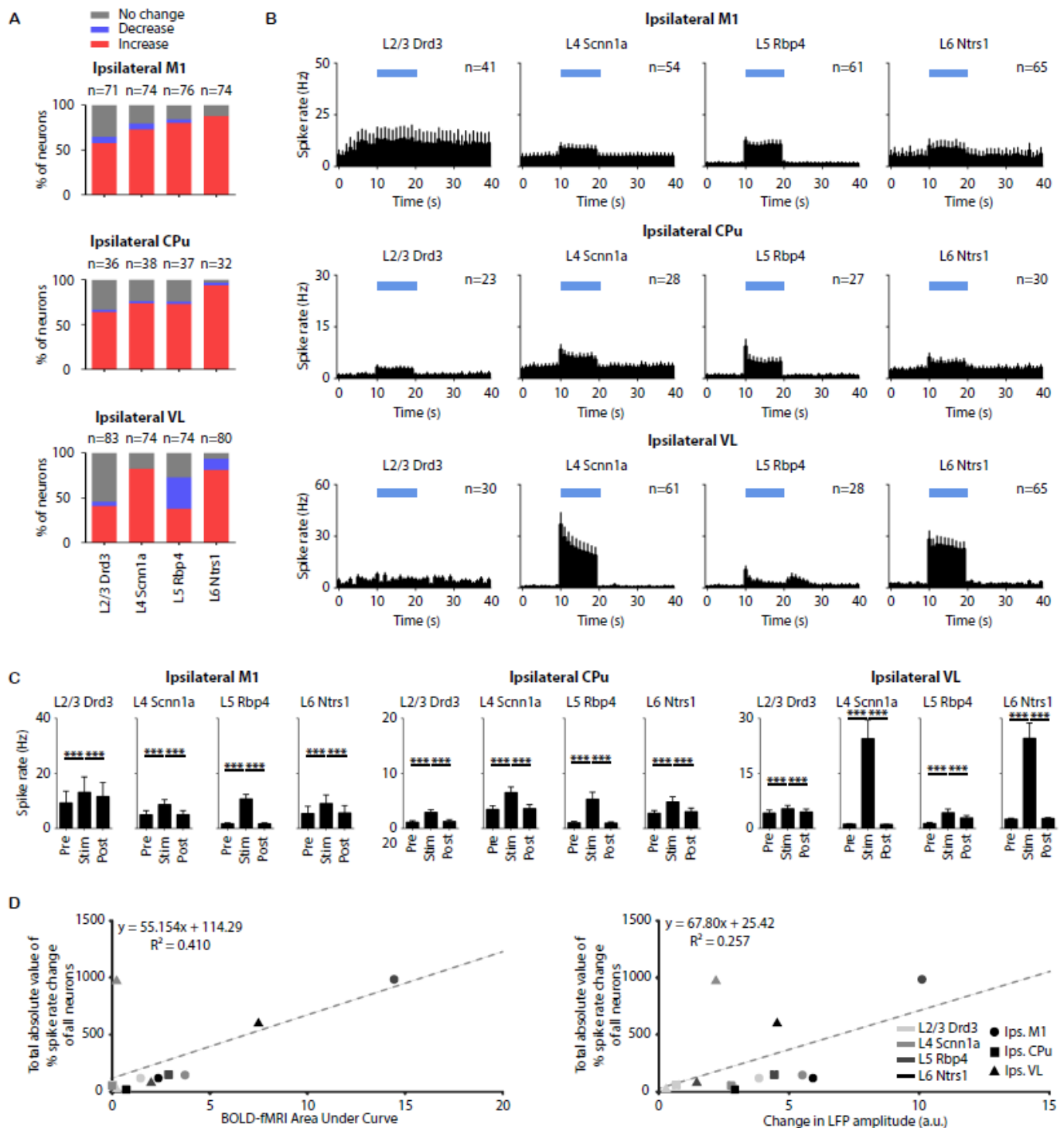


Figure 4

LFP recordings reveal activations in M1 for all layer-specific stimulations and in CPu and VL for L4, L5 and L6 stimulations only, which correlates with fMRI activations. (A) Schematic shows recording optrode and electrode locations in ipsilateral M1, CPu, and VL. (B) Average LFP (n = 4 animals per Cre-line, total N = 16 animals) from ipsilateral M1, VL, and CPu layer-specific M1 stimulation at 5 Hz shows robust activation in M1 for all Cre-lines, and in CPu and VL for Scnn1a L4, Rbp4 L5 and Ntsr1 L6 Cre-lines. (C) Change in LFP amplitude during stimulation was calculated to quantify the LFP traces. L5 stimulation evoked the strongest change in LFP amplitude in ipsilateral M1 compared to L2/3, L4 and L6 stimulations. L2/3 stimulation evoked the weakest change in LFP amplitude in ipsilateral CPu. For ipsilateral VL, L6 stimulation evoked the strongest change in LFP amplitude, while L5 and L4 stimulation evoked stronger activations compared to L2/3. These LFP results corroborate with our fMRI results. One-way ANOVA followed by Bonferroni's post hoc test was used (\*p < 0.05, \*\*p < 0.01 and \*\*\*p < 0.001; error bars indicate  $\pm$ SEM). (D) Scatter plot shows correlation between change in LFP amplitude and BOLD-fMRI area under the curve in ipsilateral M1, CPu, and VL for all Cre-lines.



**Figure 5**

Distinct spike responses and dynamics evoked by layer-specific stimulation correlating with LFP and fMRI results. (A) Quantification of significant changes in firing rate across recorded units. For each unit, paired student t-test was applied and results with  $p < 0.05$  were considered significant ( $n = 4$  animals per Cre-line, total  $N = 16$  animals). Red, blue and gray indicate units with significant increase, significant decrease and no significant change, respectively, during stimulation. Over half were modulated by all

L2/3, L4, L5 and L6 M1 stimulation at 5 Hz. Nearly all modulated units exhibited a significant increase in firing rate except for those in the ipsilateral VL during L5 and L6 stimulations. (B) Mean peri-event time histograms across all units with significant increased firing rates in the ipsilateral M1, CPU and VL during layer-specific stimulation. Robust increase in spike rates were observed in the ipsilateral M1 and CPU during L2/3, L4, L5 and L6 stimulation, while robust increase in spike rate in ipsilateral VL was only observed during L4, L5 and L6 stimulation. Error bars represent  $\pm$  SEM. (C) Average firing rates of units with significant increase before, during, and after stimulation (10 s periods, one-way ANOVA followed by Bonferroni's post hoc test; \* $p < 0.05$ , \*\* $p < 0.01$  and \*\*\* $p < 0.001$ ; error bars indicate  $\pm$ SEM). (D) Scatter plots of total absolute value of percentage spike rate change of all neurons against BOLD-fMRI area under the curve and against change in LFP amplitude in ipsilateral M1, CPU and VL for all Cre-lines show that spike rate, fMRI and LFP results are correlated.

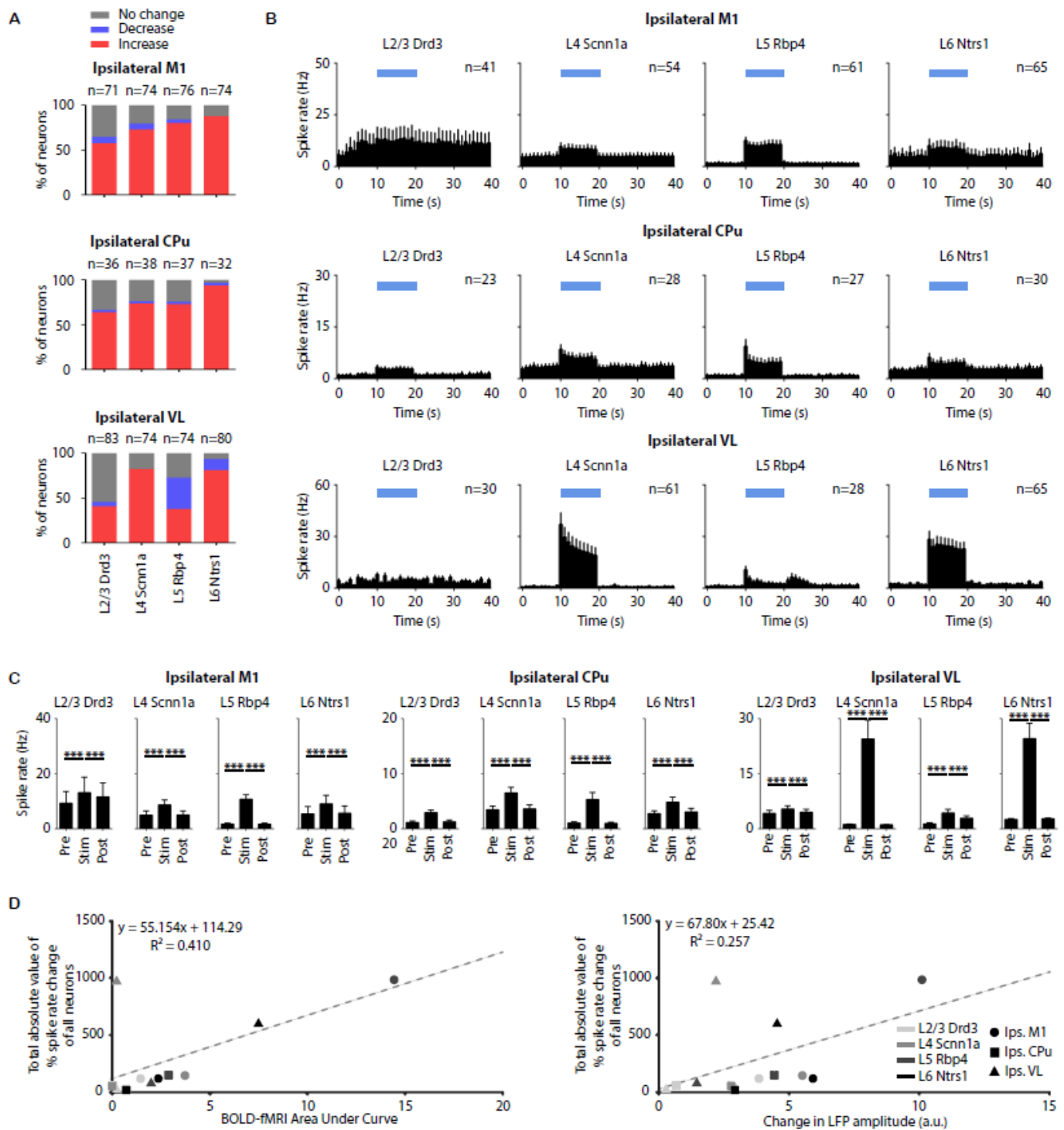


**Figure 5**

Distinct spike responses and dynamics evoked by layer-specific stimulation correlating with LFP and fMRI results. (A) Quantification of significant changes in firing rate across recorded units. For each unit, paired student t-test was applied and results with  $p < 0.05$  were considered significant ( $n = 4$  animals per Cre-line, total  $N = 16$  animals). Red, blue and gray indicate units with significant increase, significant decrease and no significant change, respectively, during stimulation. Over half were modulated by all

L2/3, L4, L5 and L6 M1 stimulation at 5 Hz. Nearly all modulated units exhibited a significant increase in firing rate except for those in the ipsilateral VL during L5 and L6 stimulations. (B) Mean peri-event time histograms across all units with significant increased firing rates in the ipsilateral M1, CPU and VL during layer-specific stimulation. Robust increase in spike rates were observed in the ipsilateral M1 and CPU during L2/3, L4, L5 and L6 stimulation, while robust increase in spike rate in ipsilateral VL was only observed during L4, L5 and L6 stimulation. Error bars represent  $\pm$  SEM. (C) Average firing rates of units with significant increase before, during, and after stimulation (10 s periods, one-way ANOVA followed by Bonferroni's post hoc test; \* $p < 0.05$ , \*\* $p < 0.01$  and \*\*\* $p < 0.001$ ; error bars indicate  $\pm$ SEM). (D) Scatter plots of total absolute value of percentage spike rate change of all neurons against BOLD-fMRI area under the curve and against change in LFP amplitude in ipsilateral M1, CPU and VL for all Cre-lines show that spike rate, fMRI and LFP results are correlated.

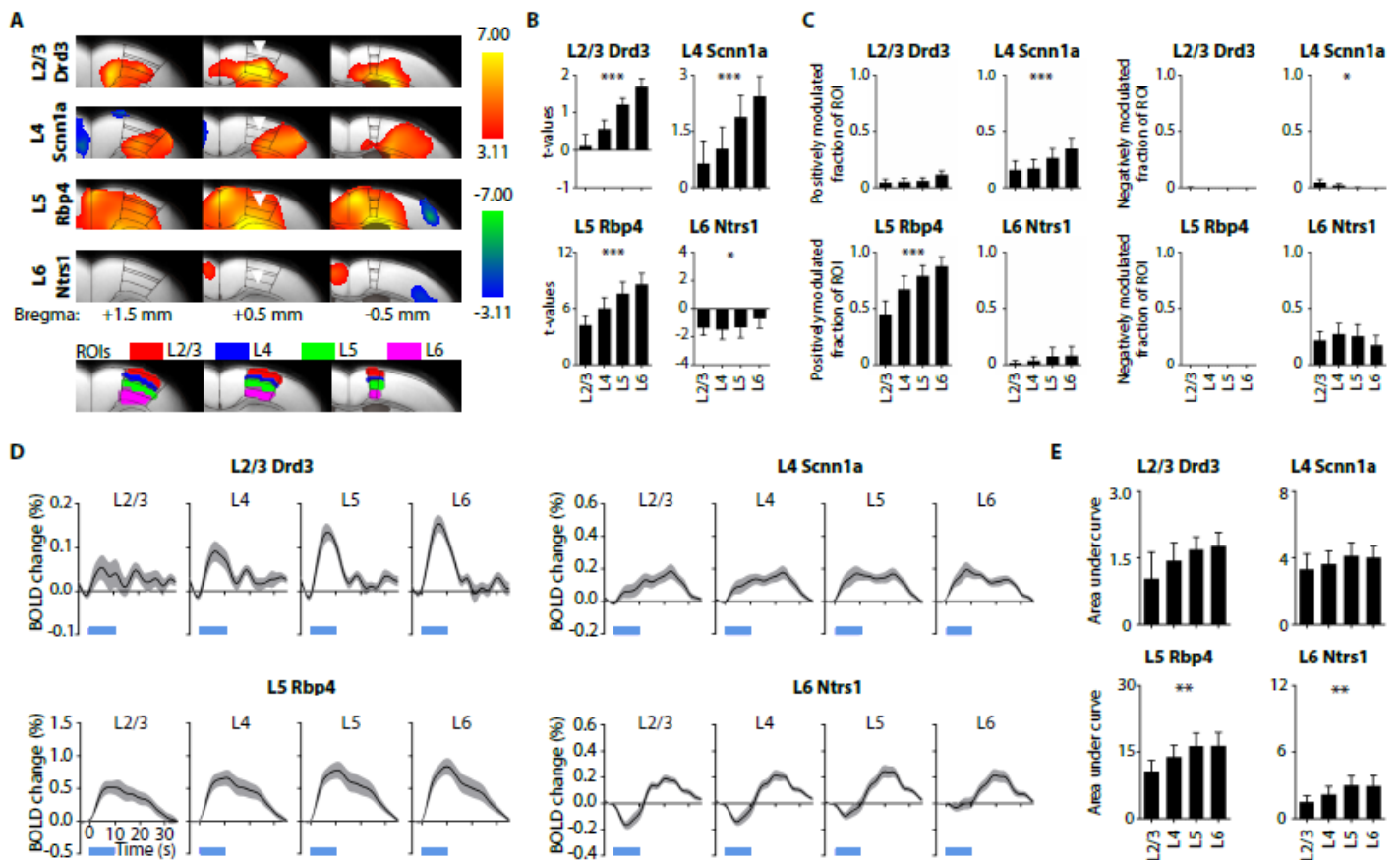


**Figure 6**

Distinct mesoscale laminar of fMRI responses evoked by layer-specific stimulation at 5 Hz exhibits a similar increasing trend along the M1 cortical depth. (A) Group-level M1 local activation maps during L2/3, L4, L5, and L6 M1 stimulation at 5 Hz ( $n=12$  animals per Cre-line, total  $N = 48$  animals;  $p < 0.001$ , FDR-corrected). Distinct mesoscale laminar fMRI responses were observed. Inverted triangle indicate site of stimulation; warm and cool colors indicate positive and negative t-scores, respectively. Regions of interest (ROIs; bottom) were defined based on the mouse brain atlas to quantify the layer-specific activations at the local ipsilateral M1. (B) Extracted t-values for the comparison of fMRI responses

across different layers. Although all fMRI responses were distinct, they exhibit a similar increasing trend along the cortical depth for all layer-specific stimulations. (C) Extracted fraction of ROI positively (left) and negatively (right) modulated for the comparison of ofMRI responses across different layers. Fraction of ROI positively modulated exhibit an increasing trend along the cortical depth during L4 and L5 stimulations, while fraction of ROI negatively modulated exhibit a decreasing trend along the cortical depth during L4 stimulation. (D) BOLD signal profiles extracted from the ROIs. These BOLD signal profiles also appears to exhibit an increasing trend along the cortical depth. (E) Area under the curve (AUC) was calculated from the extracted BOLD profiles for the comparison across different layers. AUC exhibit an increasing trend along the cortical depth during L5 and L6 stimulations. One-way ANOVA followed by trend analysis was applied (\* $p < 0.05$ , \*\* $p < 0.01$  and \*\*\* $p < 0.001$ ). Error bars indicate  $\pm$ SEM.

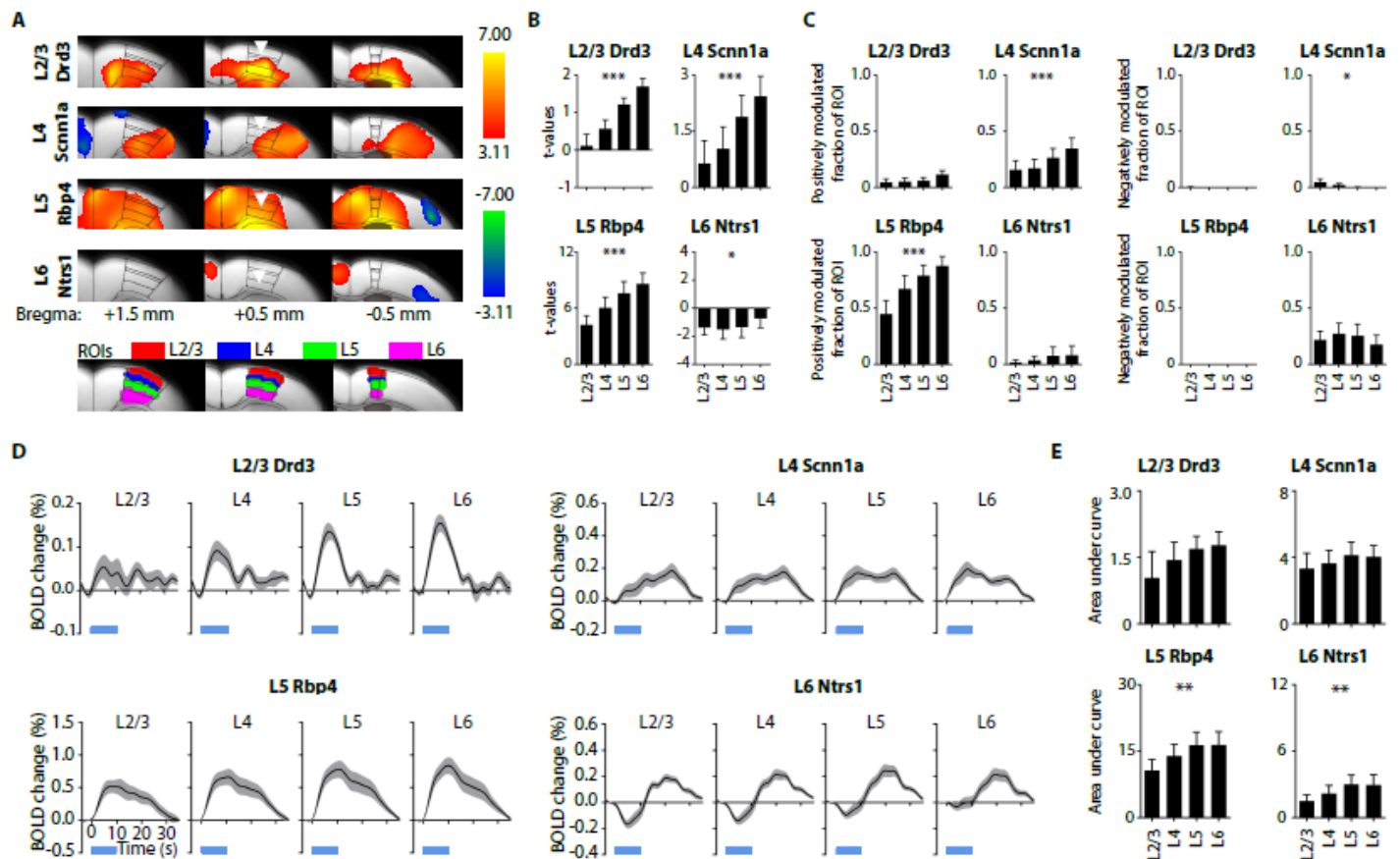


**Figure 6**

Distinct mesoscale laminar ofMRI responses evoked by layer-specific stimulation at 5 Hz exhibits a similar increasing trend along the M1 cortical depth. (A) Group-level M1 local activation maps during L2/3, L4, L5, and L6 M1 stimulation at 5 Hz ( $n=12$  animals per Cre-line, total  $N = 48$  animals;  $p < 0.001$ , FDR-corrected). Distinct mesoscale laminar fMRI responses were observed. Inverted triangle indicate site of stimulation; warm and cool colors indicate positive and negative t-scores, respectively. Regions of interest (ROIs; bottom) were defined based on the mouse brain atlas to quantify the layer-specific activations at the local ipsilateral M1. (B) Extracted t-values for the comparison of ofMRI responses across different layers. Although all fMRI responses were distinct, they exhibit a similar increasing trend

along the cortical depth for all layer-specific stimulations. (C) Extracted fraction of ROI positively (left) and negatively (right) modulated for the comparison of fMRI responses across different layers. Fraction of ROI positively modulated exhibit an increasing trend along the cortical depth during L4 and L5 stimulations, while fraction of ROI negatively modulated exhibit a decreasing trend along the cortical depth during L4 stimulation. (D) BOLD signal profiles extracted from the ROIs. These BOLD signal profiles also appears to exhibit an increasing trend along the cortical depth. (E) Area under the curve (AUC) was calculated from the extracted BOLD profiles for the comparison across different layers. AUC exhibit an increasing trend along the cortical depth during L5 and L6 stimulations. One-way ANOVA followed by trend analysis was applied (\* $p < 0.05$ , \*\* $p < 0.01$  and \*\*\* $p < 0.001$ ). Error bars indicate  $\pm$ SEM.

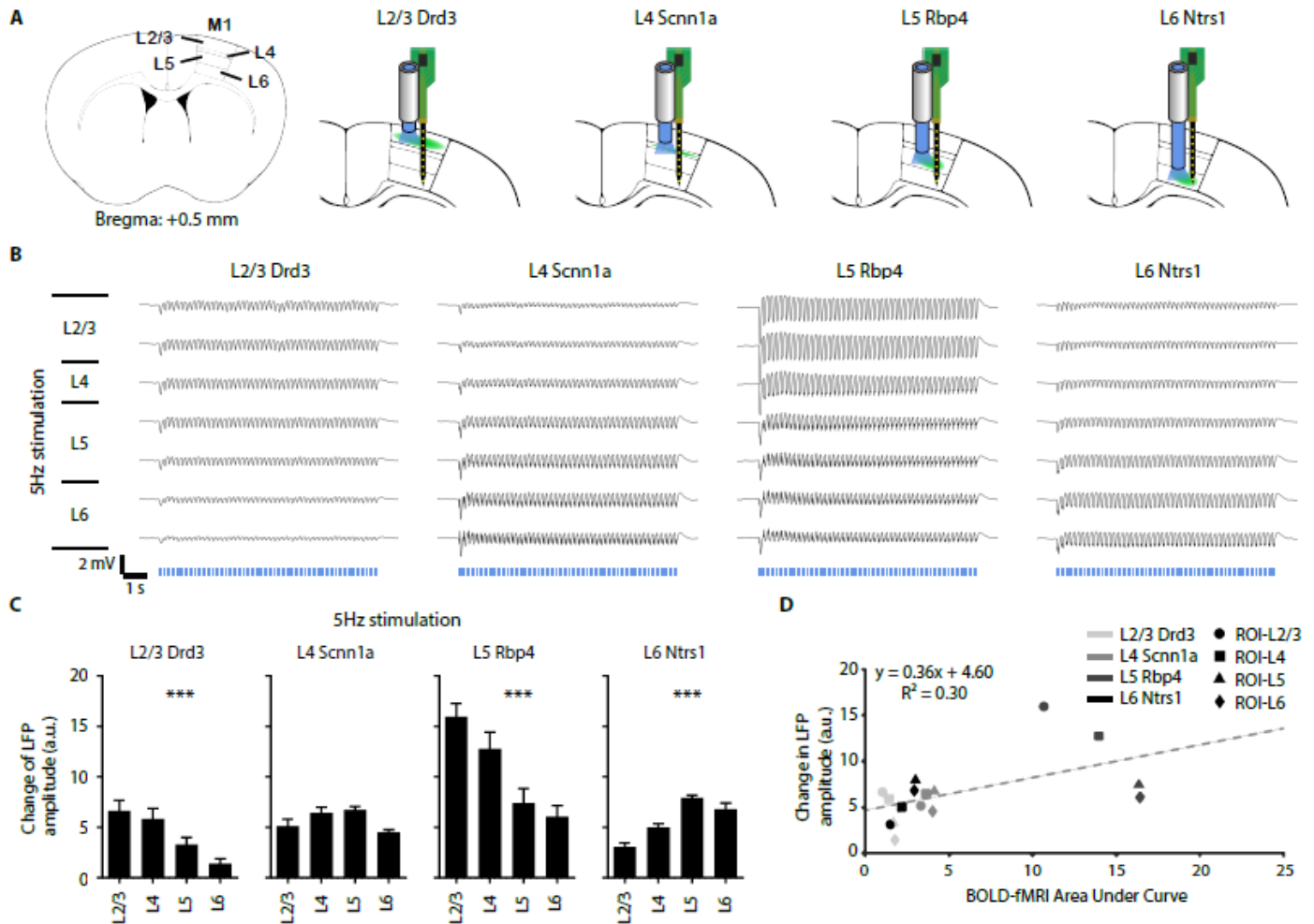


**Figure 7**

Distinct laminar LFP recordings along M1 cortical depth reveal layer-specific activations at respective layer-specific stimulations at 5 Hz which correlates with laminar fMRI responses. (A) Schematic shows laminar recording optrode location in ipsilateral M1 along cortical depth. (B) Average LFP traces (n = 4 animals per Cre-line, total N = 16 animals) of ipsilateral M1 along cortical depth at 5 Hz layer-specific optogenetic stimulation. (C) Change in LFP amplitude during stimulation was calculated to quantify the LFP traces. The change in LFP amplitude decreased along the cortical depth during L2/3 and L5 stimulation, while the amplitude increased along the cortical depth during L4 and L6 stimulation. One-way

ANOVA followed by trend analysis was applied (\* $p < 0.05$ , \*\* $p < 0.01$  and \*\*\* $p < 0.001$ ). Error bars indicate  $\pm$ SEM. (D) Scatter plot of change in LFP amplitude against BOLD-fMRI area under the curve along the cortical depth in ipsilateral M1 for all Cre-lines shows that our LFP and fMRI results are correlated.

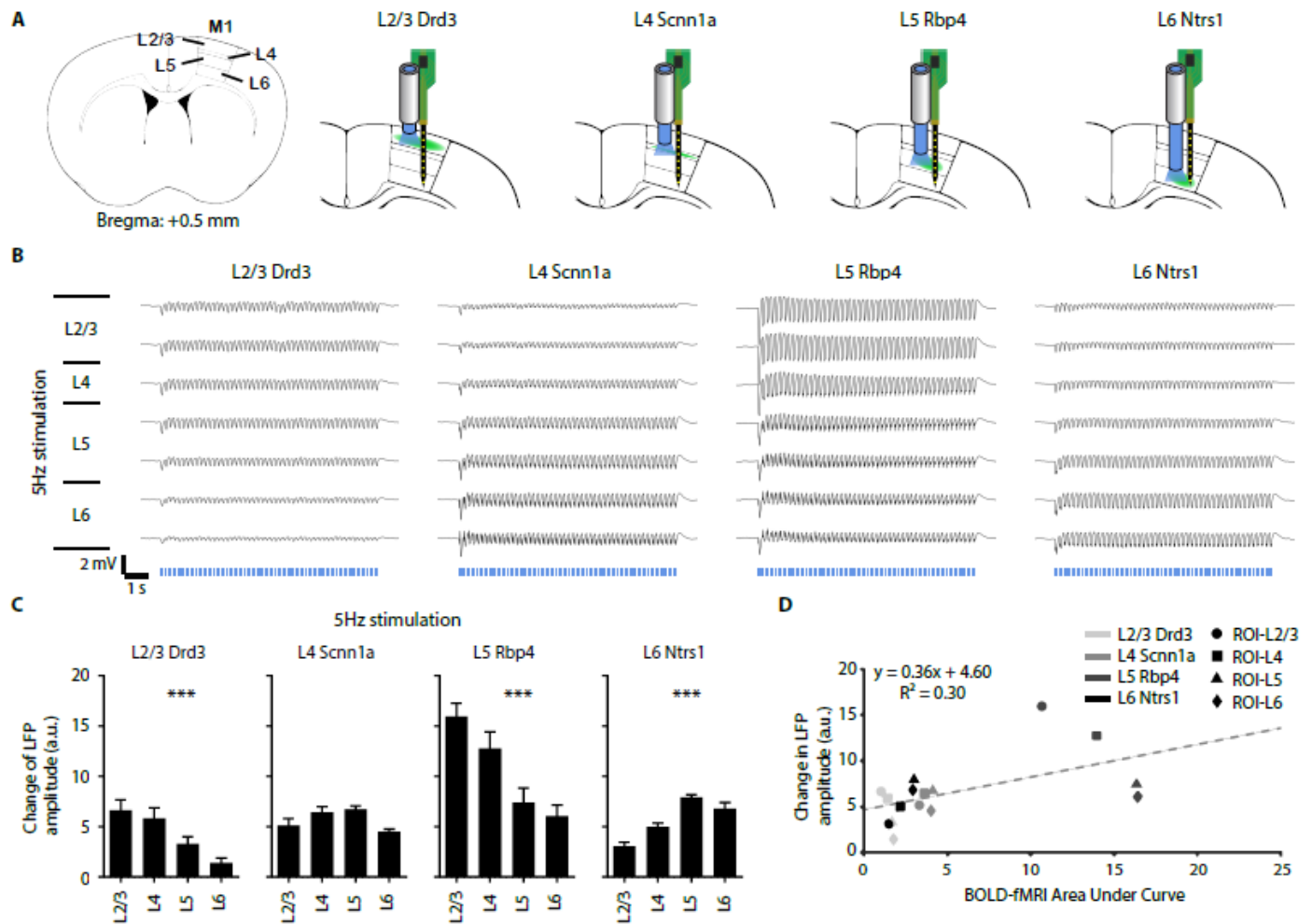


**Figure 7**

Distinct laminar LFP recordings along M1 cortical depth reveal layer-specific activations at respective layer-specific stimulations at 5 Hz which correlates with laminar fMRI responses. (A) Schematic shows laminar recording optrode location in ipsilateral M1 along cortical depth. (B) Average LFP traces (n = 4 animals per Cre-line, total N = 16 animals) of ipsilateral M1 along cortical depth at 5 Hz layer-specific optogenetic stimulation. (C) Change in LFP amplitude during stimulation was calculated to quantify the LFP traces. The change in LFP amplitude decreased along the cortical depth during L2/3 and L5 stimulation, while the amplitude increased along the cortical depth during L6 stimulation. One-way ANOVA followed by trend analysis was applied (\* $p < 0.05$ , \*\* $p < 0.01$  and \*\*\* $p < 0.001$ ). Error bars indicate  $\pm$ SEM. (D) Scatter plot of change in LFP amplitude against BOLD-fMRI area under the curve along the cortical depth in ipsilateral M1 for all Cre-lines shows that our LFP and fMRI results are correlated.

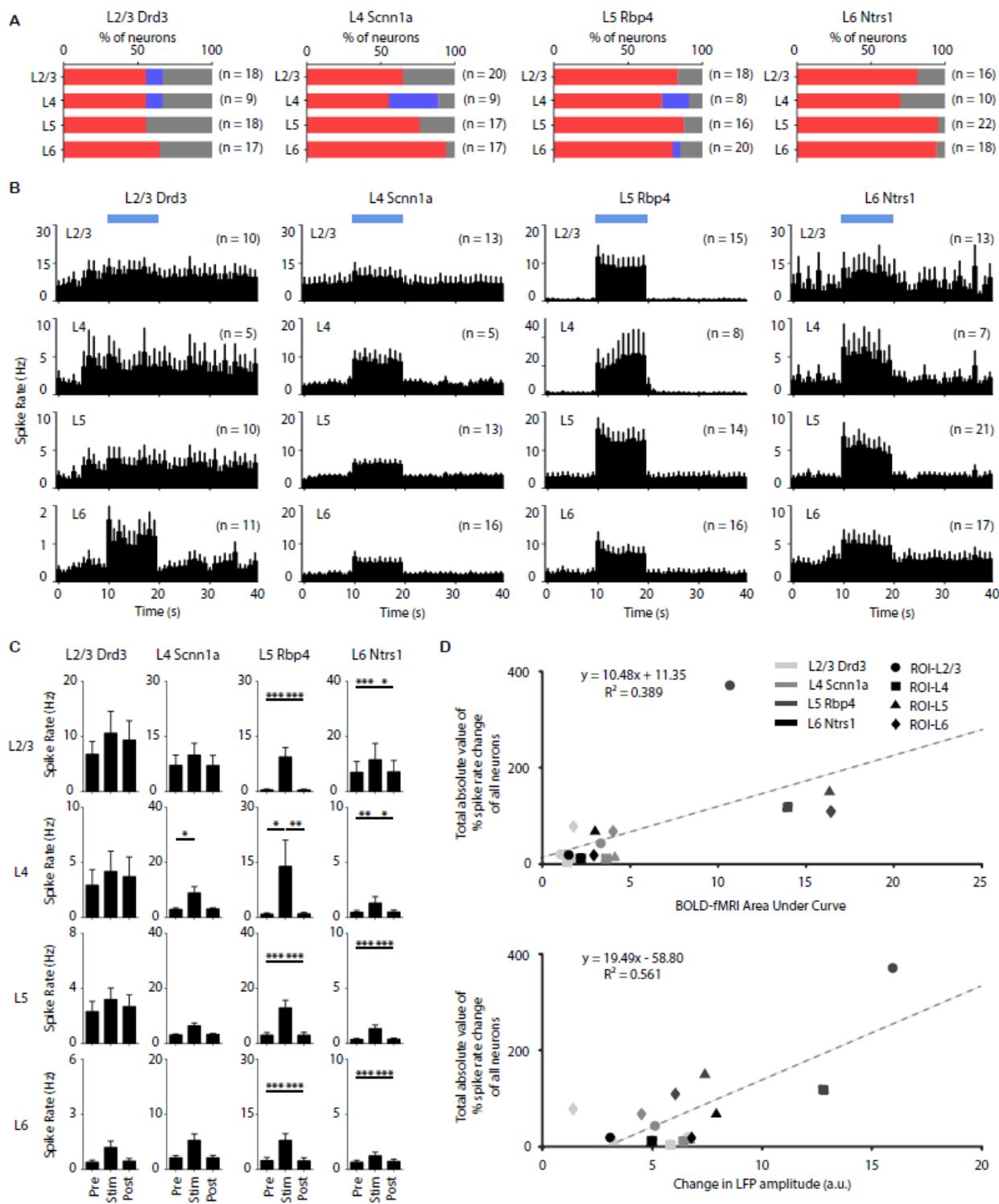


**Figure 8**

Distinct laminar spiking dynamics evoked by layer-specific M1 stimulation at 5 Hz correlating with laminar fMRI responses and change in LFP amplitude. (A) Quantification of significant changes in firing rate across recorded units. For each unit, paired student t-test was applied and results with  $p < 0.05$  were considered significant ( $n = 4$  animals per Cre-line, total  $N = 16$  animals). Red, blue and gray indicate units with significant increase, significant decrease and no significant change, respectively, during stimulation.

Over half of the recording units were modulated by the selective stimulation of each layer. Furthermore, nearly all modulated units exhibited a significant increase in firing rate. (B) Mean peri-event time histograms across all units with significant increased firing rates along ipsilateral M1 cortical depth during L2/3, L4, L5 and L6 M1 stimulation at 5 Hz. Interestingly, robust increase in spike rates was observed in L6 during L2/3 stimulation. Error bars represent  $\pm$ SEM. (C) Average firing rates of units with significant increase before, during, and after stimulation (10 s periods, one-way ANOVA followed by Bonferroni's post hoc test; \* $p < 0.05$ , \*\* $p < 0.01$  and \*\*\* $p < 0.001$ ; error bars indicate  $\pm$ SEM). (D) Scatter plots of total absolute value of percentage spike rate change of all neurons against BOLD-fMRI area under the curve and against change in LFP amplitude along the cortical depth for all Cre-lines show that spike rate, fMRI and LFP results along the cortical depth are correlated.

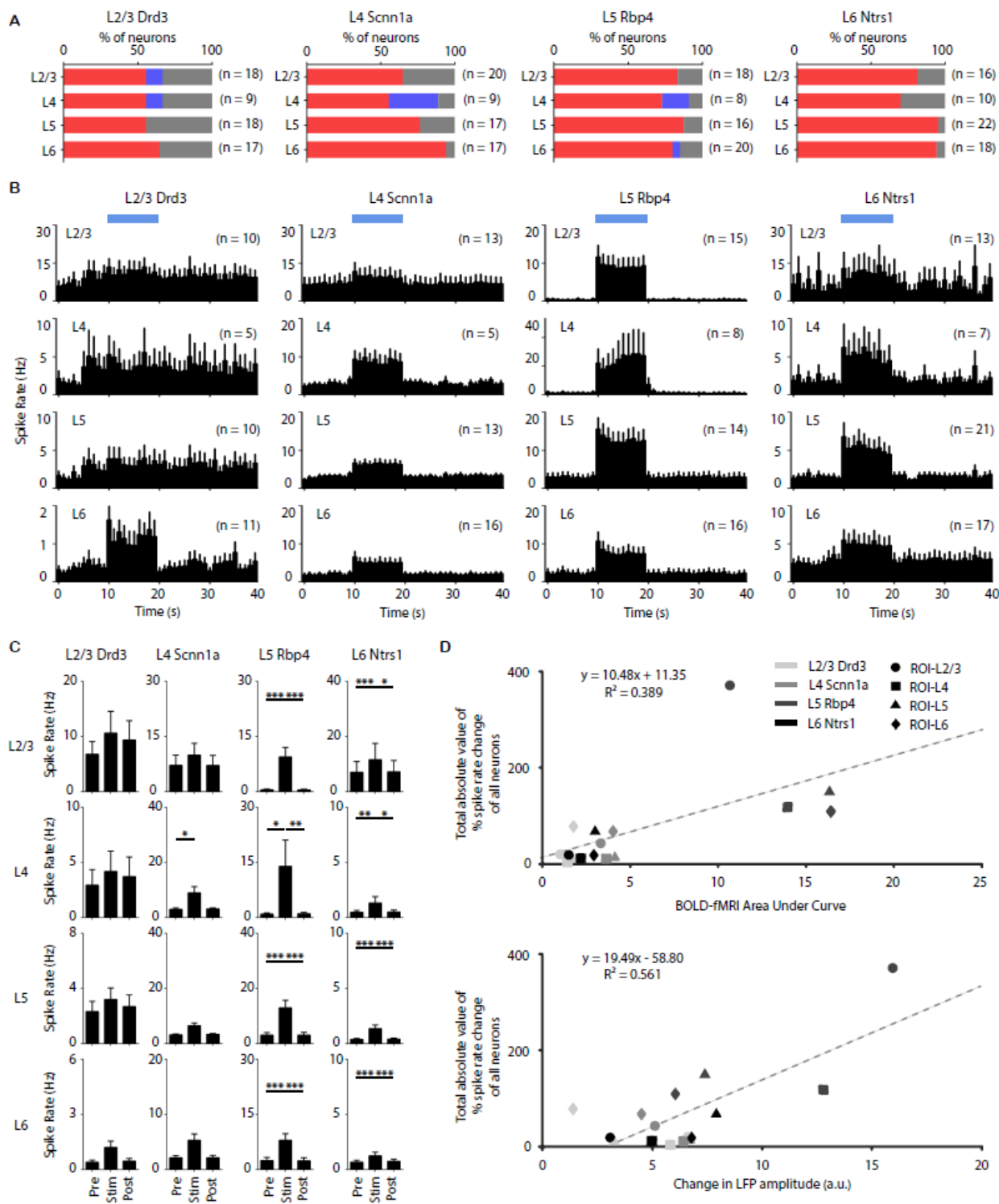


**Figure 8**

Distinct laminar spiking dynamics evoked by layer-specific M1 stimulation at 5 Hz correlating with laminar fMRI responses and change in LFP amplitude. (A) Quantification of significant changes in firing rate across recorded units. For each unit, paired student t-test was applied and results with  $p < 0.05$  were considered significant ( $n = 4$  animals per Cre-line, total  $N = 16$  animals). Red, blue and gray indicate units with significant increase, significant decrease and no significant change, respectively, during stimulation.

Over half of the recording units were modulated by the selective stimulation of each layer. Furthermore, nearly all modulated units exhibited a significant increase in firing rate. (B) Mean peri-event time histograms across all units with significant increased firing rates along ipsilateral M1 cortical depth during L2/3, L4, L5 and L6 M1 stimulation at 5 Hz. Interestingly, robust increase in spike rates was observed in L6 during L2/3 stimulation. Error bars represent  $\pm$ SEM. (C) Average firing rates of units with significant increase before, during, and after stimulation (10 s periods, one-way ANOVA followed by Bonferroni's post hoc test; \* $p < 0.05$ , \*\* $p < 0.01$  and \*\*\* $p < 0.001$ ; error bars indicate  $\pm$ SEM). (D) Scatter plots of total absolute value of percentage spike rate change of all neurons against BOLD-fMRI area under the curve and against change in LFP amplitude along the cortical depth for all Cre-lines show that spike rate, fMRI and LFP results along the cortical depth are correlated.

## Supplementary Files

This is a list of supplementary files associated with this preprint. Click to download.

- [Supplementary20201104.docx](#)
- [Supplementary20201104.docx](#)